Università di Catania

SCIENZE MATEMATICHE, FISICHE, NATURALI

---

*Roberta Farina*

# Electrochemical sensing of N compounds

*PhD thesis in Material Sciences and Nanotechnologies*
XXXVIII CYCLE

Tutor:
Prof. Guglielmo
Guido Condorelli

Co-Tutor:
SR. Sebania Libertino

---

Anno Accademico 2022 – 2025

**Publication list**

This doctoral work resulted in the publication of five peer-reviewed scientific articles in international journals, one book chapter, one proceedings paper, and the submission of an Italian patent application, PCT extended, reflecting both the scientific significance and technological innovation of the developed electrochemical sensors. The publications cover the design, fabrication, and characterization of advanced sensing platforms for nitrate, nitrite, and ammonium detection in water, both irrigation and fresh, using modified screen-printed electrodes. The published works are hereafter listed:

- Farina, R.; D'Arrigo, G.; Alberti, A.; Scalese, S.; Capuano, G.E.; Corso, D.; Screpis, G.A.; Coniglio, M.A.; Condorelli, G.G.; Libertino, S. Copper Micro-Flowers for Electrocatalytic Sensing of Nitrate Ions in Water. *Sensors* **2024**, *24*, 4501. https://doi.org/10.3390/s24144501.

- Farina, R.; D'Arrigo, G.; Alberti, A.; Capuano, G.E.; Corso, D.; Screpis, G.A.; Coniglio, M.A.; Condorelli, G.G.; Libertino, S. Electrochemical Growth of Copper Crystals on SPCE for Electrocatalysis Nitrate Reduction. *Nanomaterials* **2024**, *14*, 1704. https://doi.org/10.3390/nano14211704.

- Farina, R.; Scalese, S.; Corso, D.; Capuano, G.E.; Screpis, G.A.; Coniglio, M.A.; Condorelli, G.G.; Libertino, S. Chronoamperometric Ammonium Ion Detection in Water via Conductive Polymers and Gold Nanoparticles. *Molecules* **2024**, *29*, 3028. https://doi.org/10.3390/molecules29133028.

- Farina, R.; Scalese, S.; Alberti, A.; Privitera, S.M.S.; Capuano, G.E.; Corso, D.; Screpis, G.A.; Reina, S.C.R.; Condorelli, G.G.; Coniglio, M.A.; Condorelli, G.G.; Libertino, S. Electrocatalytical Nitrite Oxidation via Manganese and Copper Oxides on Carbon Screen-Printed Electrode. *Sensors* **2025**, *25*, 3764. https://doi.org/10.3390/s25123764.

- Capuano, G.E.; Farina, R.A.; Screpis, G.A.; Corso, D.; Coniglio, M.A.; Libertino, S. In-Situ Contaminant Detection by Portable and Potentially

Real-Time Sensing Systems. In *Environmental Sciences*; IntechOpen: London, UK, **2024**. https://doi.org/10.5772/intechopen.1006070.

- Farina, R.; Capuano, G.E.; Reina, S.C.R.; Corso, D.; Screpis, G.A.; Coniglio, M.A.; Libertino, S. Screen-Printed Electrochemical Sensor Platform for Nitrate and Nitrite Detection in Water, **2025**, IEEE International Workshop on Metrology for Green technologies, REnewable ENergy and ecological SusTainability (METROGREENST). DOI pending.

- Marino, N.; Milazzo, R.G.; Farina, R.; Bongiorno, C.; Libertino, S.; Lombardo, S.A.; Privitera, S.M.S. High-Performance Fe–MoS2 Electrocatalyst for Efficient Nitrate Reduction to Ammonia: Synergistic Design for Sustainable Ammonia Production. *ACS Sustain. Chem. Eng.* **2025**, 13, 43. https://doi.org/10.1021/acssuschemeng.5c04274.

In addition, a national patent application was filed to protect the innovative approach for nitrate sensing using copper micro-flower modified electrodes: Farina, R.; Libertino, S. Nitrates Electrocatalytic Detection in Water by Copper Microflowers. Italian Patent 102024000005344, filed on March 11, 2024. International Patent Application PCT/IB2025/052593, filed on March 11, 2025.

**TABLE OF CONTENTS**

**CHAPTER 3 – NITRITE ION SENSING**



**CHAPTER 4 – AMMONIUM ION SENSING**

**CONCLUSION**

## ABSTRACT

Monitoring the concentration of nitrate ($NO_3^-$), nitrite ($NO_2^-$), and ammonium ($NH_4^+$) ions in water is vital due to their significant environmental and health impacts. Nitrogen, essential for all living organisms, plays a key role in biological molecules such as proteins and nucleic acids. However, contamination from nitrogenous compounds, primarily due to agriculture, livestock, and wastewater, poses serious risks to aquatic ecosystems and public health. This PhD thesis centers on developing and characterizing sensitive, cost-effective, and portable electrochemical sensors for real-time detection of these ions. Utilizing screen-printing technology enables the fabrication of electrodes with reproducible chemical performance, where surface modification of the working electrode (WE) is pivotal for sensitivity and selectivity.

For nitrate detection, copper (Cu) was electrodeposited as well-defined micro-flower crystals onto carbon Screen Printed Electrodes (SPEs), leveraging its high conductivity ($5.8 \times 10^7$ S/m) to enhance charge transfer. The resulting sensor exhibits a sensitivity of 44.71 µA/mM, a low detection limit (LoD) of 0.87 µM, and a linear range from 0.05 to 3 mM, with satisfactory stability (maximum RSD 5%) and reproducibility (maximum RSD 4%). This work led to a PCT patent submission and two international journal publications.

Nitrite sensors were fabricated by co-electrodeposition of CuO and $MnO_2$ on carbon electrodes. These oxides act synergistically as catalysts for the electrooxidation of $NO_2^-$ to $NO_3^-$, providing high catalytic activity with a sensitivity of 10.83 µA/µM, a LoD of 0.071 µM, and a linear range of 0.2–60 µM. The sensor demonstrated reproducibility with a maximum standard deviation of 2.91% and repeatability for up to three uses, documented in an international journal publication.

Ammonium sensing employed conductive polymers and gold nanoparticles (AuNPs), combining the versatile polyaniline (PANI) polymer with AuNPs for efficient signal transduction. Two electrode functionalizations were performed using cyclic voltammetry: AuNP electrodeposition on commercial PANI/C electrodes (Au/PANI/C) and electropolymerization of PANI (PANIep) followed by AuNP deposition on carbon electrodes (Au/PANIep/C). The Au/PANI/C electrode shows excellent sensitivity at higher $NH_4^+$ concentrations (LoD 0.34 µM), but reduced sensitivity at lower levels (0.01 µM LoD) across 0.35 to 7 µM ranges. Conversely, Au/PANIep/C provides superior sensitivity at low concentrations (0.03 µM LoD) with a modest decrease at higher concentrations (0.07 µM LoD). Both electrodes exhibit good reproducibility, with maximum RSD values of 3.68% and 5.94%, respectively.

All sensors were evaluated against common potential interferents including $NO_3^-$, $Cl^-$, $NH_4^+$, and $NH_2Cl$, demonstrating negligible interference, confirming their selectivity and practical applicability for water quality monitoring.

**List of Abbreviations**

**Au NPs** Gold Nanoparticles

**Au/PANI/C** Carbon electrode modified with polyaniline and gold nanoparticles

**Au/PANIep/C** Carbon electrode modified with electropolymerized polyaniline and gold nanoparticles

**CA** Chronoamperometry

**CE** Counter Electrode

**Cu/C** Carbon electrode modified with copper

**Cu-Mn/C** Carbon electrode modified with copper and manganese

**CV** Cyclic Voltammetry

**EDX** Energy Dispersive X-ray Spectroscopy

**LSV** Linear Sweep Voltammetry

**LoD** Limit of Detection

**PANI/C** Commercial polyaniline/carbon electrode

**PANIep** Electropolymerized polyaniline

**RE** Reference Electrode

**RSD** Relative Standard Deviation

**SD** Standard Deviation

**SEM** Scanning Electron Microscopy

**SPCE** Screen Printed Carbon Electrodes

**SPE** Screen Printed Electrodes

**WE** Working Electrode

**WHO** World Health Organization

**XPS** X-ray Photoelectron Spectroscopy

**XRD** X-ray Diffraction

## INTRODUCTION

Nitrogen is an essential element for all living organisms, playing a central role in biological systems, especially in proteins and nucleic acids [1]. However, when nitrogen compounds accumulate excessively in aquatic environments, they can lead to serious environmental issues and pose significant health risks. The contamination of water resources by nitrogen compounds such as nitrates, nitrites, and ammonium ions is therefore considered one of the most pressing environmental challenges worldwide. These pollutants primarly originate from anthropogenic activities, especially intensive agriculture, livestock farming, and domestic wastewater discharge, and can severely impact both aquatic ecosystems and human health [2,3]. According to the World Health Organization (WHO), the maximum recommended levels in drinking water are 50 mg/L for nitrate and 3 mg/L for nitrite. The European Union also set a limit for ammonium, typically at 0.5 mg/L. Accurate and continuous monitoring of these species is essential to ensure water quality for human consumption, agricultural use, and environmental protection [4].

Although conventional analytical methods are highly sensitive and reliable, are often expensive, time-consuming, and require sophisticated instrumentation and trained personnel—factors that limit their suitability for on-site and real-time analysis. In this context, electrochemical sensors based on screen-printed electrodes have emerged as a promising alternative owing to their low cost, portability, rapid response, and potential for mass production with good reproducibility [5-7].

This thesis is organized into four main chapters, each addressing specific aspects of electrochemical sensing of nitrogen species in water. Chapter 1 lays the foundational knowledge, detailing the basic principles of electrochemical sensing and the use of screen-printed electrodes as versatile platforms for sensor

development. Chapter 2 focuses on the design, fabrication, and detailed characterization of copper-modified carbon SPEs for the electrochemical detection of nitrate ions, including morphological studies, electrochemical behavior, and sensor performance tests under various conditions. Chapter 3 presents the development of nitrite sensors based on synergistic copper and manganese oxide catalysts electro deposited onto carbon electrodes, analyzing their catalytic mechanisms, sensitivity, selectivity, and application potential. Chapter 4 explores sensor architectures for ammonium ion detection, combining conductive polymers such as polyaniline with gold nanoparticles, emphasizing different electrode fabrication strategies, morphological and electrochemical characterization, and evaluation of sensing efficacy. The concluding section summarizes the major findings, compares the developed sensors with existing technologies, and discusses future directions for implementing these systems in real-world water quality monitoring.

## REFERENCES


[1] Forde, B.G.; Clarkson, D.T. Nitrate and Ammonium Nutrition of Plants: Physiological and Molecular Perspectives. *Adv. Bot. Res.* **1999**, *30*, 1–90. https://doi.org/10.1016/S0065-2296(08)60226-8.

[2] Edwards, T.M.; Puglis, H.J.; Kent, D.B.; López Durán, J.; Bradshaw, L.M.; Farag, A.M. Ammonia and Aquatic Ecosystems—A Review of Global Sources, Biogeochemical Cycling, and Effects on Fish. *Sci. Total Environ.* **2024**, *907*, 167911. https://doi.org/10.1016/j.scitotenv.2023.167911.

[3] Picetti, R.; Deeney, M.; Pastorino, S.; Miller, M.R.; Shah, A.; Leon, D.A.; Dangour, A.D.; Green, R. Nitrate and Nitrite Contamination in Drinking Water and Cancer Risk: A Systematic Review with Meta-Analysis. *Environ. Res.* **2022**, *210*, 112988. https://doi.org/10.1016/j.envres.2022.112988.

[4] Li, D.; Xu, X.; Li, Z.; Wang, T.; Wang, C. Detection Methods of Ammonia Nitrogen in Water: A Review. *TrAC Trends Anal. Chem.* **2020**, *127*, 115890. https://doi.org/10.1016/j.trac.2020.115890.

[5] Hanrahan, G.; Patil, D.G.; Wang, J. Electrochemical Sensors for Environmental Monitoring: Design, Development and Applications. *J. Environ. Monit.* **2004**, *6*, 657–664. https://doi.org/10.1039/b403975k.

[6] Yáñez-Sedeño, P.; Campuzano, S.; Pingarrón, J.M. Electrochemical (Bio)Sensors: Promising Tools for Green Analytical Chemistry. *Curr. Opin. Green Sustain. Chem.* **2019**, *19*, 1–7. https://doi.org/10.1016/j.cogsc.2019.01.004.

[7] Yáñez-Sedeño, P.; Campuzano, S.; Pingarrón, J.M. Screen-Printed Electrodes: Promising Paper and Wearable Transducers for (Bio)Sensing. *Biosensors* **2020**, *10*(7), 76. https://doi.org/10.3390/bios10070076.

# CHAPTER 1

# FUNDAMENTALS OF ELECTROCHEMICAL SENSING AND SCREEN-PRINTED ELECTRODES

## 1- Fundamentals of Electrochemistry

Electrochemistry is the scientific field that investigates the relationship between electrical energy and chemical transformations. The fundamental processes in electrochemistry are redox (reduction-oxidation) reactions, which involve the transfer of electrons between chemical species. In a redox reaction, one species loses electrons (oxidation) while another gains electrons (reduction).

Central to this process is the electrochemical cell composed of three electrodes: a working electrode (WE), where the analyte undergoes site-specific oxidation or reduction; a reference electrode (RE) to ensure the precise application of the WE potential; and a counter electrode (CE) to complete the circuit [1]. Redox reactions facilitate the conversion of chemical interactions into quantifiable electrical signals, such as current, potential, or impedance, which are directly proportional to the concentration of the target analyte. The driving force for redox reactions is the difference in electrochemical potential between the reactants and products [2]. This potential difference can be described quantitatively by the Nernst equation (Eq. 1), which relates the electrode potential to the concentrations of the chemical species involved:

$$E = E^0 + \frac{RT}{nF} \ln \frac{[Ox]^a}{[Red]^b} \qquad (1)$$

where $E$ is the electrode potential, $E^0$ is the standard electrode potential, $R$ is the gas constant, $T$ is the temperature in Kelvin, $n$ is the number of electrons transferred, $F$ is the Faraday constant, *[Ox]* and *[Red]* are the concentrations of

the oxidized and reduced forms, respectively, while *a* and *b* are the stoichiometric coefficients of *[Ox]* and *[Red]*.

The current produced, resulting from the change in oxidation state of the electroactive species, is termed the Faradaic current because it obeys Faraday's law (that is, the reaction of 1 mole involves a change of n x 96,485.33 C). The Faradaic current is a direct measure of the rate of redox reaction. The rate at which these redox reactions occur at an electrode is governed by two main factors: charge-transfer kinetics and mass transport. Charge-transfer kinetics refer to the intrinsic ability of electrons to move between the electrode and the redox species. This is described by the Butler-Volmer equation, which relates the current to the applied potential, the standard rate constant, and the concentrations of the reactants at the electrode surface [3]. The rate constant for electron transfer depends on the electronic structure of the electrode material, the nature of the redox species (such as the energies of their HOMO/LUMO orbitals), and the structure of the solution. Mass transport refers to how quickly the reactant species reach the electrode surface from the bulk solution. This can occur via diffusion (movement due to concentration gradients), migration (movement in response to an electric field), or convection (bulk movement of the solution). In most practical electrochemical systems, diffusion is the dominant mode of mass transport, especially when a supporting electrolyte is present to minimize migration effects. Depending on the relative rates of these two processes, the overall reaction can be:

- Kinetically controlled: If the electron transfer at the electrode is slow compared to the arrival of reactants by diffusion, the current is determined by the charge-transfer kinetics. In this case, the concentration of reactant at the electrode surface is nearly equal to that in the bulk solution, and the reaction rate increases with increasing overpotential.

- Diffusion-controlled (mass transport-controlled): If the electron transfer is very fast, the reactant is consumed as soon as it reaches the electrode surface. The rate-limiting step becomes the diffusion of reactant from the bulk solution to the electrode. Here, the current is determined by the diffusion coefficient, the concentration gradient, and the thickness of the diffusion layer.

In real systems, there can be mixed control, where both charge-transfer kinetics and mass transport influence the reaction rate. The interplay between these factors determines whether a reaction is reversible (fast kinetics, limited by diffusion) or irreversible (slow kinetics, limited by electron transfer) [4].

## 2- Electrochemical Sensing Techniques

Electrochemical sensors utilize various measurement techniques to analyze the interaction of analytes with the electrode surface. The three main techniques used in this thesis are: cyclic voltammetry (CV), linear sweep voltammetry (LSV), and chronoamperometry (CA) [5].

Cyclic Voltammetry applies a triangular potential waveform to the working electrode, sweeping linearly between two set potentials in a cyclic manner. This method is indispensable for characterizing redox-active materials, as the resulting voltammogram displays oxidation and reduction peaks that reveal reaction reversibility, electron transfer kinetics, and surface adsorption processes [6]. The peak separation ($\Delta Ep$) and peak current ratios ($I_{pa}/I_{pc}$) provide insights into reaction mechanisms, while the peak potential (Ep) correlates with the formal reduction potential ($E^o$) of the analyte.

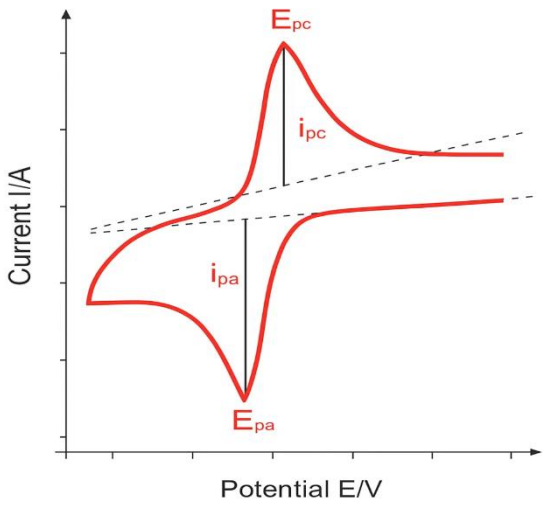


Figure 1. Typical cyclic voltammogram for a reversible redox process, where $E_{pa}$ and $E_{pc}$ correspond to the potential values at which the maximum anodic and cathodic peak currents ($i_{pa}$ and $i_{pc}$ respectively) are recorded.

Linear Sweep Voltammetry employs a unidirectional potential sweep, typically from a lower to a higher potential, to drive analyte-specific oxidation or reduction. Unlike CV, LSV does not reverse the sweep direction, making it ideal for analytical quantification. The peak current ($I_p$) in LSV is directly proportional to analyte concentration, as described by the Randles-Ševčík equation (Eq. 2):

$$i_p = -2.69 \times 10^5 \, n^{\frac{3}{2}} A D_0^{\frac{1}{2}} v^{\frac{1}{2}} C \qquad (2)$$

where $i_p$ is the peak current, $n$ is the number of electron transfers, $A$ is the active surface area ($cm^2$), $D_o$ is the diffusion coefficient, $v$ is the scan rate ($Vs^{-1}$), and $C$ is the analyte concentration (mol $cm^{-3}$) [1]. The Randles-Ševčík equation is a tool in electrochemistry that allows us to relate three key parameters: surface area, diffusion coefficient, and redox concentration [7-9].

Chronoamperometry (CA) applies a fixed potential step to initiate redox reactions, measuring the transient current response over time. The current decay follows the Cottrell equation (Eq. 3):

$$I\ (t) = \frac{nFAC\sqrt{D}}{\sqrt{\pi t}} \qquad (3)$$

where $t$ is the time, $n$ is the number of electron transfers, $F$ is the Faraday constant, $A$ is the active surface area ($cm^2$), $D$ is the diffusion coefficient, and $C$ is the analyte concentration ($mol \cdot cm^{-3}$).

This diffusion-controlled process enables highly sensitive detection of trace electroactive species, as the initial current is proportional to analyte concentration. The CA temporal resolution is particularly advantageous for studying reaction kinetics, adsorption-desorption phenomena, and catalytic processes at modified electrode surfaces [10].

### 3- Screen Printed Electrodes (SPEs)

Screen-Printed Electrodes (SPEs) are miniaturized electrochemical sensing platforms fabricated by depositing conductive and insulating inks onto flat substrates such as plastic, ceramic, or paper using a layer-by-layer screen-printing process. These devices integrate the three-electrode system: working electrode, reference electrode, and counter electrode, into a single compact unit, enabling rapid and cost-effective analysis with minimal sample volumes (in the µL range) [10].

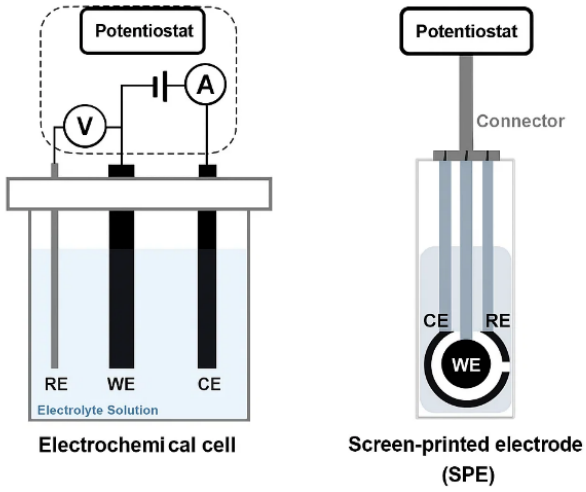


Figure 2. Screen Printed Electrodes (SPE).

The properties of the electrochemical cell are determined by the composition of the inks used during printing, while surface functionalization of the working electrode plays a critical role in enhancing the sensitivity and selectivity of the sensor for specific target analytes. The WE can be modified with a wide range of materials, including metal nanoparticles, metal oxides, organic molecules, and conducting polymers, to improve its electrochemical performance [11]. During sensing, the system undergoes an electrochemical reaction that induces measurable changes in current, potential, charge, conductivity, or impedance, depending on the technique employed. The miniaturized design of SPEs makes them suitable for portable, on-site applications and real-time monitoring, minimizing the need for large volumes of reagents and samples. Their small size, linear response, low power consumption, fast response time, high sensitivity, and ability to operate at room temperature make them ideal for the development of compact, field-deployable electrochemical sensing systems [12].

## REFERENCES


[1] O'Mullane, A.P. Electrochemistry. In *Reference Module in Chemistry, Molecular Sciences and Chemical Engineering*; Elsevier: Amsterdam, The Netherlands, **2013**. https://doi.org/10.1016/B978-0-12-409547-2.05344-0.

[2] Schwarz, K.; Sundararaman, R. The Electrochemical Interface in First-Principles Calculations. *Surf. Sci. Rep.* **2020**, *75*(2), 100492. https://doi.org/10.1016/j.surfrep.2020.100492.

[3] Nazmutdinov, R.R.; Shermokhamedov, S.A.; Zinkicheva, T.T.; Ulstrup, J.; Xiao, X. Understanding Molecular and Electrochemical Charge Transfer: Theory and Computations. *Chem. Soc. Rev.* **2023**, *52*, 18, 6454–6495. https://doi.org/10.1039/D2CS00006G.

[4] Baharfar, M.; Hillier, A.C.; Mao, G. Charge-Transfer Complexes: Fundamentals and Advances in Catalysis, Sensing, and Optoelectronic Applications. *Adv. Mater.* **2024**, *36*, 2406083. https://doi.org/10.1002/adma.202406083.

[5] Baranwal, J.; Barse, B.; Gatto, G.; Broncova, G.; Kumar, A. Electrochemical Sensors and Their Applications: A Review. *Chemosensors* **2022**, *10*, 363. https://doi.org/10.3390/chemosensors10090363.

[6] Elgrishi, N.; Rountree, K.J.; McCarthy, B.D.; Rountree, E.S.; Eisenhart, T.T.; Dempsey, J.L. A Practical Beginner's Guide to Cyclic Voltammetry. *J. Chem. Educ.* **2018**, *95*, 197–206. https://doi.org/10.1021/acs.jchemed.7b00361.

[7] Hamzah, I.H.; Abd Manaf, A.; Sidek, O. A Study on Characteristic and Reliability of Fabricated Microfluidic Three Electrodes Sensor Based on Randles-Ševčík Equation. In *Proceedings of the 2010 IEEE Asia Pacific Conference on Circuits and Systems (APCCAS 2010)*, Kuala Lumpur, Malaysia, 6–9 December 2010; pp. 816–819. https://doi.org/10.1109/APCCAS.2010.5774816.

[8] Abdi, Z.; Vandichel, M.; Sologubenko, A.S.; Willinger, M.-G.; Shen, J.-R.; Allakhverdiev, S.I.; Najafpour, M.M. The Importance of Identifying the True Catalyst When Using Randles–Ševčík Equation to Calculate Turnover Frequency. *Int. J. Hydrog. Energy* **2021**, *46*, 37774–37781. https://doi.org/10.1016/j.ijhydene.2021.09.063.

[9] González-Meza, O.A.; Larios-Durán, E.R.; Gutiérrez-Becerra, A.; Casillas, N.; Escalante, J.I.; Bárcena-Soto, M. Development of a Randles–Ševčík-like Equation to Predict the Peak Current of Cyclic Voltammetry for Solid Metal Hexacyanoferrates. *J. Solid State Electrochem.* **2019**, *23*, 3123–3133. https://doi.org/10.1007/s10008-019-04410-6.

[10] Hanrahan, G.; Patil, D.G.; Wang, J. Electrochemical Sensors for Environmental Monitoring: Design, Development and Applications. *J. Environ. Monit.* **2004**, *6*, 657–664. https://doi.org/10.1039/b403975k.

[11] Paimard, G.; Ghasali, E.; Baeza, M. Screen-Printed Electrodes: Fabrication, Modification, and Biosensing Applications. *Chemosensors* **2023**, *11*, 113. https://doi.org/10.3390/chemosensors11020113.

[12] Antuña-Jiménez, D.; González-García, M.B.; Hernández-Santos, D.; Fanjul-Bolado, P. Screen-Printed Electrodes Modified with Metal Nanoparticles for Small Molecule Sensing. *Biosensors* **2020**, *10*, 9. https://doi.org/10.3390/bios10020009.

# CHAPTER 2

# NITRATE ION SENSING

## 1- Introduction and State of the Art

Nitrates are stable, highly water-soluble nitrogen compounds that represent the predominant oxidized form of nitrogen in natural systems. While essential for plant growth, nitrates become harmful contaminants when present in excessive concentrations in water bodies. Their primary sources include nitrogen-based fertilizers, animal waste, and wastewater discharges. Beyond their ecological effects, such as eutrophication, high nitrate levels in drinking water are associated with serious health risks, including methemoglobinemia and potential links to cancer.

Electrochemical sensors have emerged as powerful tools for the detection of $NO_3^-$ in aqueous environments, leveraging various transduction mechanisms including potentiometric, amperometric, and conductometric approaches. Among the diverse electrode materials explored, copper, platinum, silver, and gold have been extensively studied due to their favorable catalytic and electrochemical properties [1, 2]. For instance, a flexible screen-printed amperometric sensor functionalized with electrodeposited copper nanoclusters on silver working electrodes demonstrated remarkable sensitivity, achieving a LoD of 0.207 nM and a dynamic linear range from 0.05 to 0.5 mM, as measured by linear sweep voltammetry [3]. Similarly, nitrate detection has been investigated using commercial single-walled carbon nanotube (SWCNT)-modified copper and palladium-copper electrodes in acidic media, yielding an extended concentration range from 0.1 to 7.8 mM and an LoD of 52 μM [1]. These studies underscore the potential of combining nanostructured materials with screen-printed electrodes to develop sensitive, cost-effective, and portable sensors. Building upon this foundation, this work focuses

on the electrochemical deposition of copper micro-flower structures onto commercially available carbon SPEs via cyclic voltammetry, aiming to fabricate a low-cost, high-performance nitrate sensor.

This chapter presents the development and characterization, including structural and electrochemical, of an SPE-based electrochemical sensor for the detection of nitrate ions in water.

## 2- Materials and Methods

To develop the nitrate sensor, a screen-printed electrode was used, consisting of a carbon working electrode, a silver reference electrode, and a platinum counter electrode. Carbon WEs offer several advantages, including low cost, high versatility, and ease of surface modification. The sensor was fabricated by modifying the carbon WE with copper. Cu is an attractive material for electrocatalytic nitrate reduction due to its high electrical conductivity ($5.8 \times 10^7$ S/m), cost-effectiveness, and excellent catalytic properties [3]. When copper is electrodeposited in the form of microcrystalline "flower-like" structures composed of metallic Cu and copper oxides ($Cu_2O$, CuO), its catalytic performance is further enhanced [4,5]. The presence of copper oxides, such as $Cu_2O$, can further modulate the electronic structure of the catalyst, promoting key intermediates in $NO_3^-$ reduction [6]. These micro-flower morphologies present a high density of edges, tips, and defects, which serve as abundant and highly reactive active sites for $NO_3^-$ adsorption and its subsequent reduction [7,8]. The increased surface area and exposure of under-coordinated copper atoms at these sites facilitate more efficient electron transfer between the electrode and nitrate ions [9]. Functionalization of the working electrode was carried out by cyclic voltammetry. Sensor performance was examined by linear sweep voltammetry.

### 3- Cu/C electrodes fabrication

Electrode preparation was performed via cyclic voltammetric electrodeposition of copper according to the functionalization schematic shown in Figure 1. Copper was electrochemically deposited onto a carbon WE (diameter 4 mm) by performing 2, 5, 7, 10, 12, and 15 potential cycles between 1.0 V and 0.0 V at a scan rate of 0.1 $Vs^{-1}$ [10]. The deposition was carried out in an unstirred electrolyte solution containing 0.1 M $CuSO_4$ and 0.1 M KCl [11].

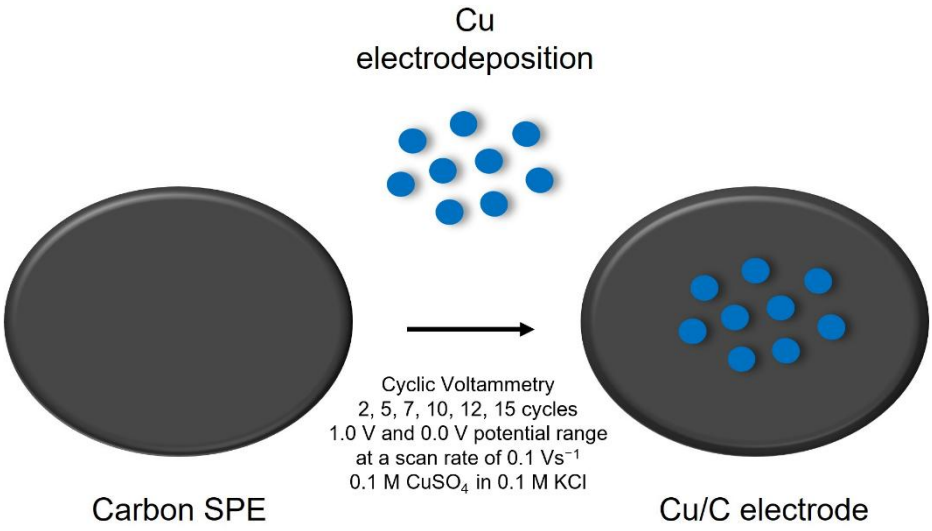


Figure 1. *S*chematic representation of the Cu/C electrode functionalization process.

Each CV cycle lasted approximately 2 minutes. During the cathodic scan (toward more negative potentials), $Cu^{2+}$ ions in solution were reduced to metallic copper, leading to its deposition on the electrode surface. During the anodic (reverse) scan, a portion of the deposited copper could be re-oxidized, depending on the scan parameters and potential limits. This deposition process generated a variety of copper morphologies on the carbon surface, influenced by the number of cycles performed [10].

## 4- Morphological and compositional characterization of Cu/C electrodes

Scanning electron microscopy (SEM) was used to investigate the morphology of copper deposited on carbon WE subjected to 2, 5, 7, 10, 12, and 15 cycles of cyclic voltammetry. After 2 cycles (Figure 2a), copper deposition appeared non-uniform, with the underlying carbon surface still widely uncovered. In contrast, 5 cycles (Figure 2b) resulted in a more homogeneous distribution of copper across the electrode surface and the uncovered surface is strongly reduced but still present. After 7 cycles, larger copper crystallites form, although parts of the carbon substrate remain exposed (Figure 2c). After 10, 12, and 15 cycles, the carbon surface is almost completely covered by merged copper structures, indicating extensive cluster growth (Figure 2d-f).

Higher magnification SEM images (Figure 3) revealed the evolution of copper morphology with increasing deposition cycles. Flower-like crystalline structures were already evident after 2 cycles (Figure 3a) and became more defined and oriented after 5 cycles (Figure 3b). These micro-flowers exhibited high surface-to-volume ratios and preserved porosity, facilitating enhanced electrochemical accessibility for $NO_3^-$ detection. However, from 7 cycles onward, the copper structures grew denser and more swollen, with evident nucleation centers along preferred crystallographic orientations (Figure 3c).

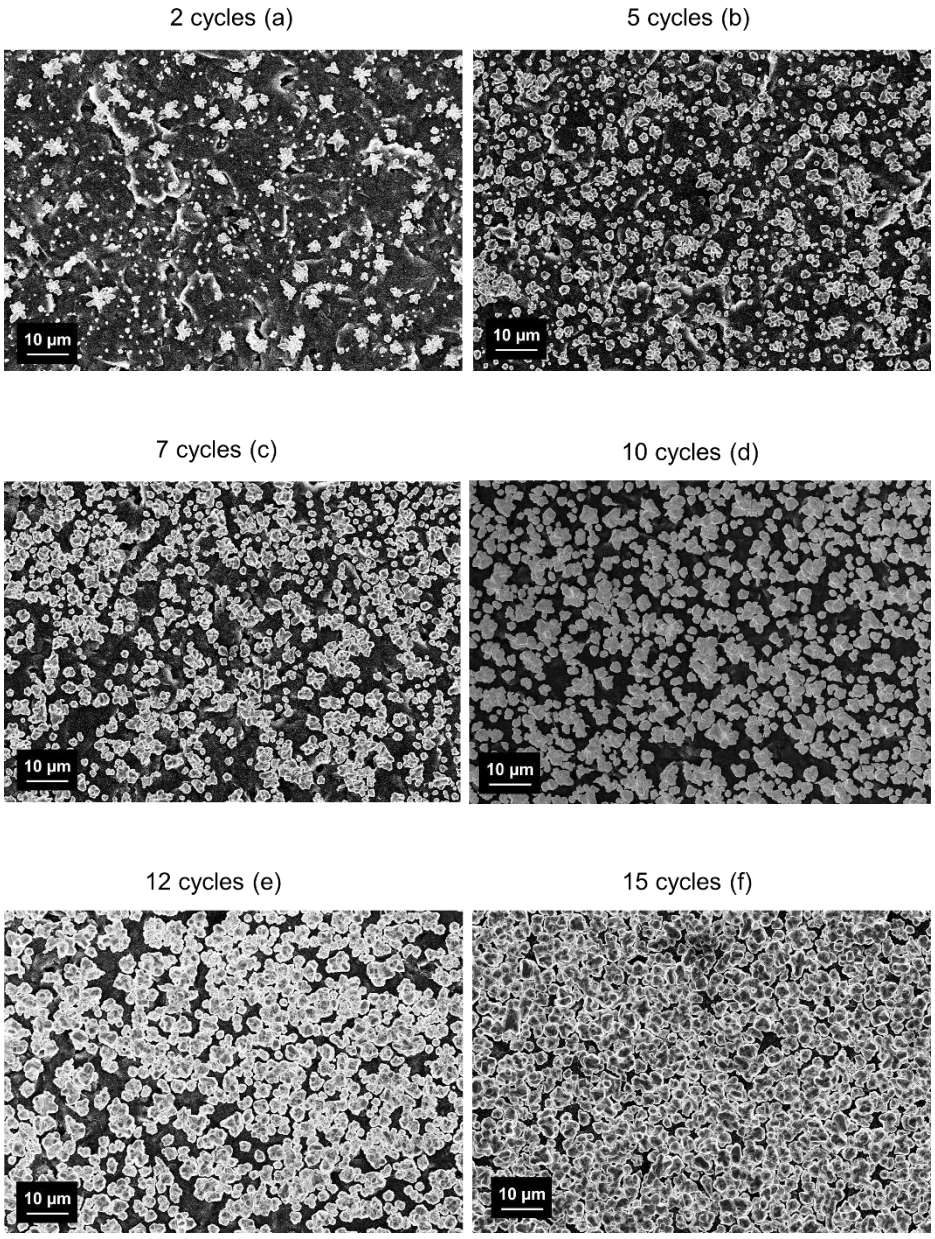


Figure 2. SEM images of C electrodes modified with (a) 2, (b) 5, (c) 7, (d) 10, (e) 12, (f) 15 cycles of Cu electrodeposition.

By increasing the number of deposition cycles (Figure 3d–f), the formation of large Cu clusters led to a reduction in electroactive sites and full carbon surface coverage.

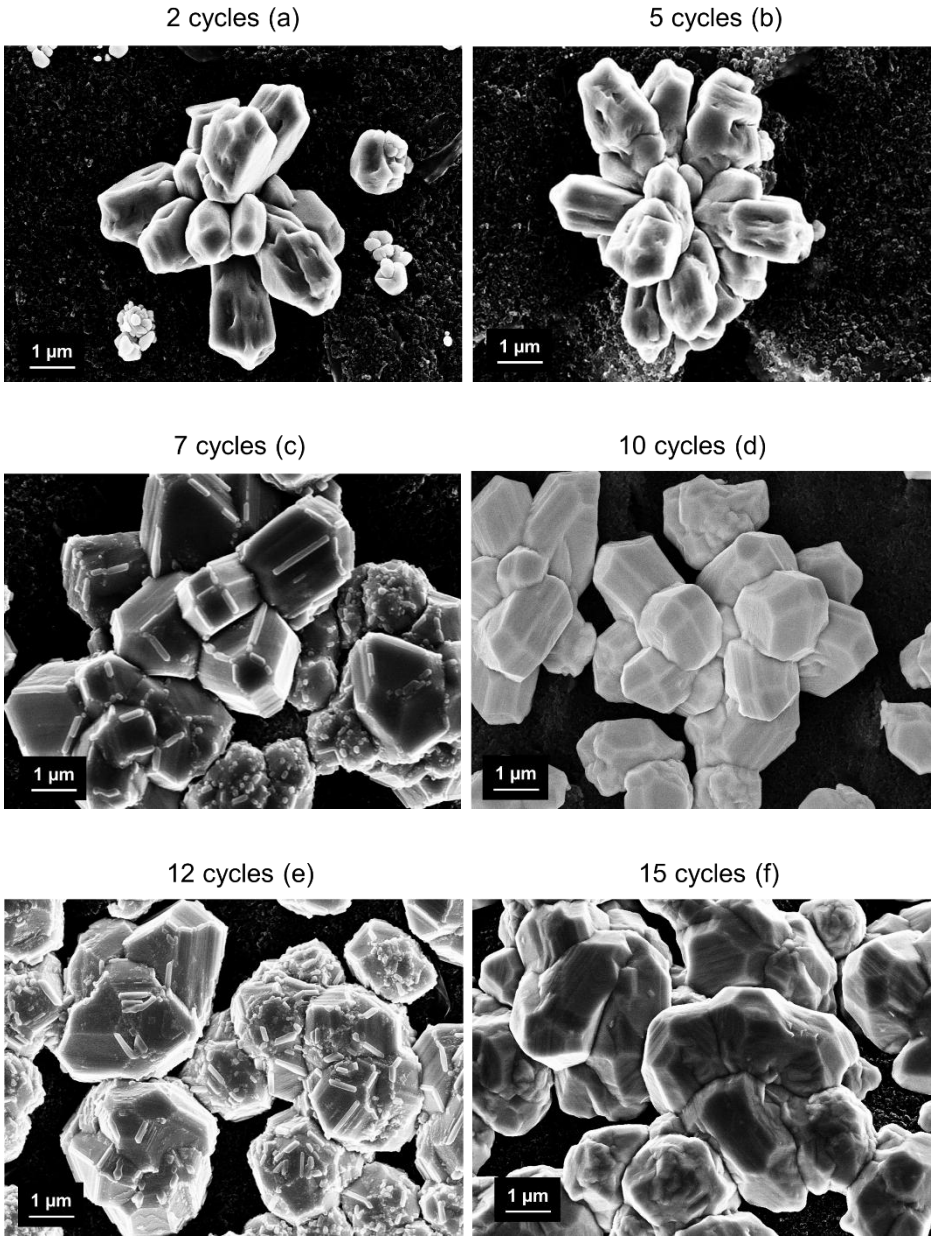


Figure 3. High-magnification SEM images of C electrodes modified with (a) 2, (b) 5, (c) 7, (d) 10, (e) 12, (f) 15 cycles of Cu electrodeposition.

These morphological changes significantly influence the electrocatalytic properties and effective surface area of the electrodes. At higher number of

deposition cycles, the crystallites already formed act as nucleation centers along the crystal orientation; this phenomenon promotes the formation of larger clusters, thus reducing the active surface area. Therefore, variations in crystal shape and structure result in different active sites and affect charge/mass transfer [12,13]. The flower-like structure of the crystallites, grown after 5 CV cycles, favors a greater catalytic effect. Their formation is associated with anion-induced directional growth of Cu crystal planes; this effect fully exposes the active sites and increases the synergistic catalytic efficiency as specifically shaped electrocatalysts can expose distinct crystal facets, enhancing both activity and selectivity for nitrate reduction due to differences in adsorption energy of intermediate species [14,15].

To further analyze the surface composition, energy-dispersive X-ray spectroscopy (EDS or EDX) was conducted on both the unmodified SPCE and the Cu/C-modified electrode after 5 CV cycles.

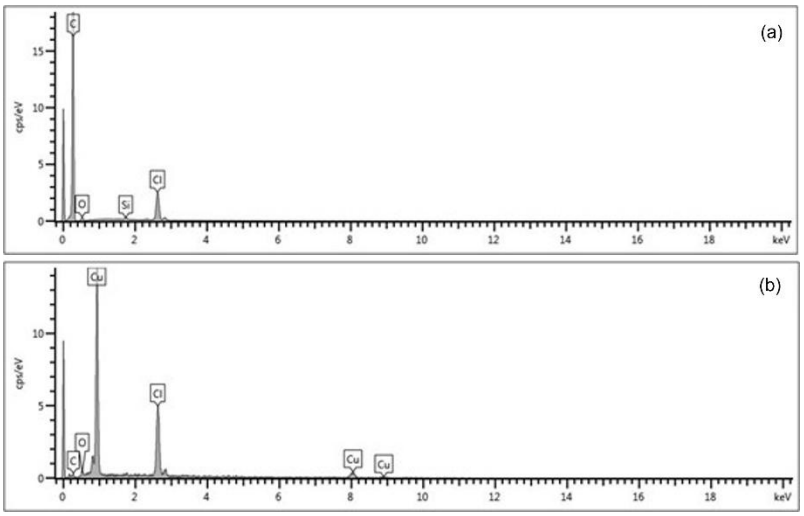


Figure 4. EDS of (a) bare SPCE and (b) Cu/C-modified electrode after 5 CV cycles.

The bare SPCE consisted mainly of carbon (90.40 wt%), along with small amounts of oxygen (2.54 wt%), silicon (0.36 wt%), and chlorine (6.86 wt%) (Figure 4a). After 5 cycles of Cu electrodeposition, the composition shifted to 70.05 wt% Cu, 21.10 wt% Cl, 6.98 wt% C, and 1.88 wt% O (Figure 4b), confirming extensive copper deposition. Notably, the percentage values obtained for each element provide an average surface composition, since the Cu structures are not forming a fully homogeneous and flat coverage on the bare carbon WE. Hence, the obtained values are in the expected range and reveal that most of the electrode surface is covered with electrodeposited Cu.

The electrodes modified with the various deposition cycles were characterized by X-ray diffraction (XRD) to evaluate their crystallographic structure. Figure 5 shows the XRD pattern comparison of the bare SPCE electrode (black trace) and the modified ones. The 2 cycles modified Cu/C electrode (purple trace in Figure 5a) shows peaks at $2\theta$ = 39.76°, 47.46°, and 54.60° corresponding to the Bragg reflections of crystalline CuO(002), CuCl(220), and CuO(020) respectively [15]. The pattern of 5 cycles Cu/C modified electrode (blue trace in Figure 5b) shows peaks at $2\theta$=50.48°, and 74.13° corresponding to the Bragg reflections of crystalline Cu(200), and Cu(220), and peaks at $2\theta$ = 36.18°, 39.76°, and 47.46° corresponding to CuO(002), CuO(022), and CuO(-202), respectively. The peak at 46.3° corresponds to CuCl(220). Therefore, the 5-cycle Cu/C modified electrode shows three additional peaks, corresponding to metallic copper and a different CuO lattice. Cu/C electrodes after 7 cycles (light blue trace) and 10 cycles (green trace) show similar patterns to the 5-cycles modified electrode (Figures 5c-d).

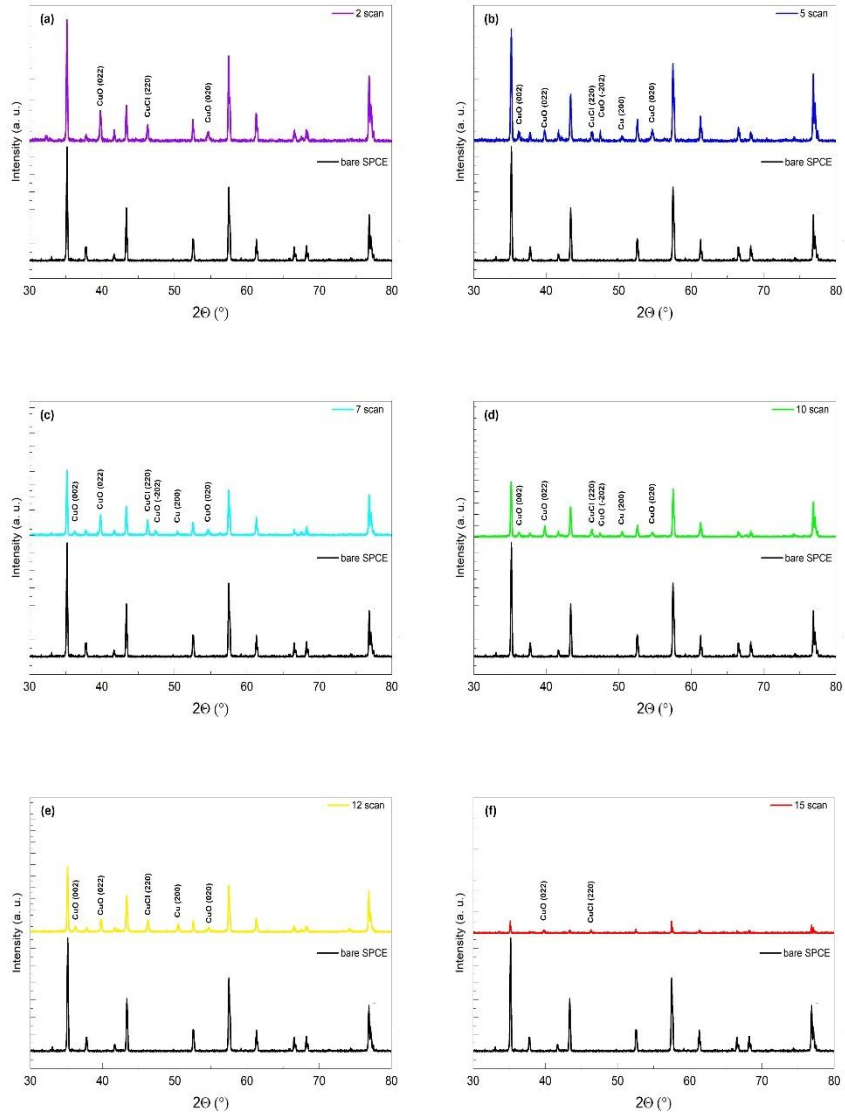


Figure 5. XRD pattern of bare SPCE (black trace) and: (a) 2 cycles (purple trace); (b) 5 cycles (blue trace); (c) 7 cycles (light blue trace); (d) 10 cycles (green trace); (e) 12 cycles (yellow trace); (f) 15 cycles (red trace) of Cu electrodeposited electrodes.

The absence of the CuO(-202) peak is observed in 12-cycles pattern (yellow trace in Figure 5e). Finally, the 15-cycles pattern (red trace) shows only peaks related to CuO(022) and CuCl(220) crystal structures (Figure 5f).

Different crystallographic orientations have different surface energies, which affect the thermodynamic stability, the ability to adsorb nitrate iones, and the reactivity. Surfaces with lower surface energies tend to be more stable but less reactive, while those with higher energies may be more reactive. Furthermore, different crystallographic orientations offer different densities of active sites, influencing the number of sites available for the catalytic reaction. Therefore, a surface with a higher density of exposed copper atoms can adsorb nitrates more effectively. Metallic copper is known to facilitate nitrate reduction due to its high electrical conductivity and availability of conduction electrons [1,2,16]. Conversely, the presence of chlorine can negatively influence the active sites nature and their interaction with nitrates. The obtained patterns confirm the successful coverage of crystalline Cu on top of the carbon WE [18]. Additionally, the observation aligns with those of Inam et al. [3] and Chen et al. [18] who demonstrated that the morphology of Cu electrocrystallization is controlled by the surface energies of the crystallographic planes.

Raman analysis of the SPCE after 2, 5, 7, 10, and 15 CV copper electrodeposition cycles was performed (Figure 6). The spectra show distinct differences between the bare carbon electrode and the modified electrodes. The Raman shift range (300-1200 $cm^{-1}$) primarily captures the vibrational modes associated with copper oxide species, as the characteristic carbon D and G bands appear at higher wavenumbers (~1350 and ~1580 $cm^{-1}$). The prominent peaks observed around 520-560 $cm^{-1}$ and 610-630 $cm^{-1}$ can be attributed to $Cu_2O$, usually characterized by peaks around 520-540 $cm^{-1}$, and CuO, usually associated with peaks around 290-300 $cm^{-1}$ and 610-630 $cm^{-1}$.

The slight shifts and intensity changes in these peaks across samples with different deposition cycles suggest an increase in copper oxide presence on the electrode surface as the number of functionalization cycles increases, likely due to

progressive oxidation or greater incorporation of copper oxides into the carbon electrode surface.

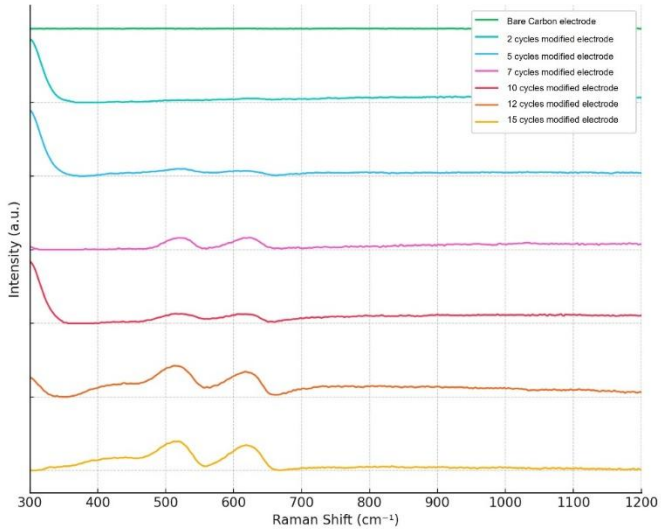


Figure 6. Raman spectra of bare (green line) SPCEs and modified with 2 (greenish line), 5 (light blue line), 7 (magenta line), 10 (red line), 12 (orange line), and 15 (yellow line) cycles of Cu electrodeposition.

X-ray photoelectron spectroscopy (XPS) analysis provide a flat line for the bare SPCE, indicating no copper species are present on the unmodified electrode surface (red line, Figure 7). The spectra of the modified electrodes show well-defined Cu2p peaks, confirming successful copper/copper oxides deposition on the carbon surface. The intensity of the peaks increases moderately with additional deposition cycles. The peak position at 932.8 eV is consistent with either metallic copper or $Cu_2O$, which cannot be distinguished by Cu2p XPS alone due to their similar binding energies. The absence of prominent satellite peaks (in the 940-945 eV region) suggests that Cu(II) species (e.g., CuO) are not dominant in these samples.

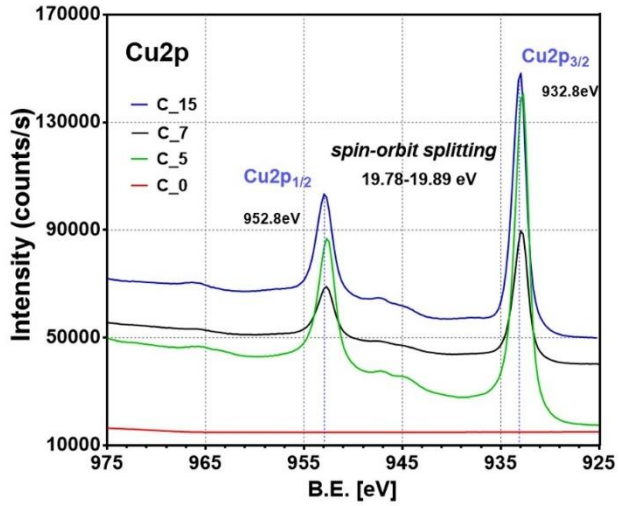


Figure 7. XPS spectra of electrodes: SPCE bare (red line), Cu/C electrodes modified with 5 (green line), 7 (black line), and 15 (blue line) cycles of Cu electrodeposition.

This interpretation aligns with the XRD results, which detected various copper species, including CuO and CuCl, on the modified electrodes, with different crystalline structures forming depending on the number of deposition cycles. In addition, the relatively strong signal indicates a significant copper coverage, consistent with SEM images showing uniform distribution of Cu atoms over the entire carbon electrode surface.

## 5- Electrochemical characterization of Cu/C electrodes

Electrochemical characterization of the bare and copper modified carbon electrodes was performed in a 0.1 M KCl electrolyte solution, both in the absence (Figure 8a) and in the presence of nitrate to a concentration of 1.6 mM (Figure 8b). In the electrolyte solution, the bare SPCE (black dash-dash trace) exhibits the $C_0$ wave characteristic of the electrode, which becomes smoother in the case of the copper-modified electrode. This wave remains unchanged in the presence of nitrate, demonstrating the bare carbon electrode inactivity towards nitrate ions.

Figure 8a shows the voltammograms corresponding to the different deposition cycle numbers. They exhibit two cathodic peaks at −0.33 V ($C_1$) and −0.75 V ($C_2$). $C_1$ and $C_2$ are associated with the reduction of Cu(I) and Cu(II), as illustrated by Equations (1) and (2). Their presence indicates the successful coating of the carbon WE [19].

$$Cu(I) + e^- \rightarrow Cu \qquad (1)$$

$$Cu(II) + 2e^- \rightarrow Cu \qquad (2)$$

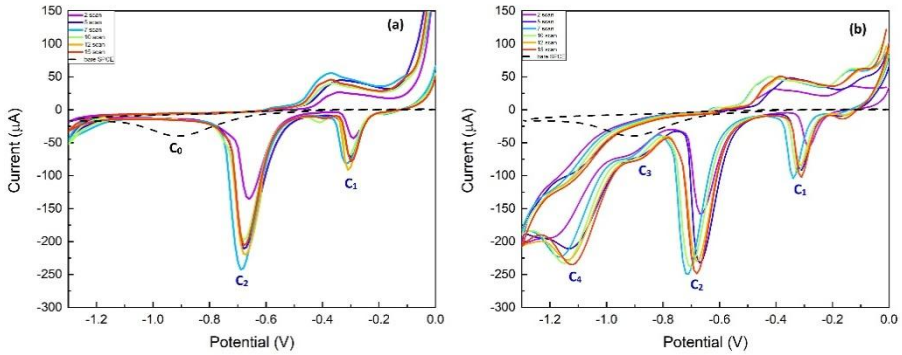


Figure 8. CV in 0.1 M KCl of (a) bare C electrode (black dash-dash trace) and Cu/C modified electrodes: 2 cycles (purple trace), 5 cycles (blue trace), 7 cycles (light-blue trace), 10 cycles (green trace), 12 cycles (yellow trace), 15 cycles (red trace); (b) same electrodes in the presence of nitrate (1.6 mM $NO_3^-$).

In the presence of 1.6 mM $NO_3^-$ (Figure 8b), two additional reduction peaks at -0.86 V ($C_3$) and -1.08 V ($C_4$) appear in the cyclic voltammograms of the Cu/C modified electrodes. $C_3$ and $C_4$ denote the diffusion currents related to the reduction of $NO_3^-$ and $NO_2^-$ [19]. These reactions are illustrated by Equations (3) and (4).

$$NO_3^- + H_2O + 2e^- \rightarrow NO_2^- + 2OH^- \quad (3)$$

$$NO_2^- + 5H_2O + 2e^- \rightarrow NH_3 + 7OH^- \quad (4)$$

The obtained results agree with those reported by Inam et al.[3], and Lotfi Zadeh Zhad et al. [20].

To optimize the Cu deposition process each electrode was examined via LSV in four different $NO_3^-$ solutions (0.1, 0.8, 1.6, and 3 mM).

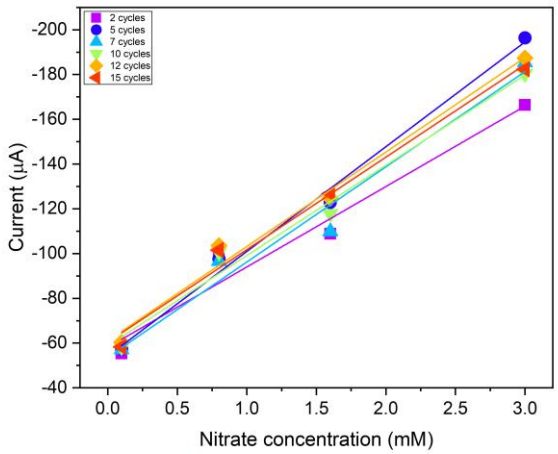


Figure 9. Calibration curves of the electrodes obtained for different electrodeposition cycles as a function of nitrate concentration (0.1, 0.8, 1.6 and 3 mM): 2 cycles (violet squares), 5 cycles (blue dots), 7 cycles (light blue triangles), 10 cycles (green triangles), 12 cycles (yellow squares), 15 cycles (red triangles). The points indicate the cathodic current peak at –0.86 V, while the solid lines (same color as points) represent the linear best fit of the data.

Figure 9 shows the reduction current peak at – 0.86 V of the six developed electrodes plotted against $NO_3^-$ concentration. The electrodes show different sensitivities to nitrate ions electroreduction depending on the deposition process.

| Electrodes | Sensitivity | Surface Area ($cm^2$) |
|---|---|---|
| Bare C | - | 0.0197 |
| 2 cycles | 35.94 μA/mM | 0.0854 |
| 5 cycles | 46.80 μA/mM | 0.1079 |
| 7 cycles | 42.19 μA/mM | 0.0981 |
| 10 cycles | 41.33 μA/mM | 0.0942 |
| 12 cycles | 42.53 μA/mM | 0.1001 |
| 15 cycles | 40.32 μA/mM | 0.0853 |

Table 1. Sensitivity and calculated surface area of the different electrodes

Table 1 shows the measured sensitivity for each electrode. The results indicated that 5 CV cycles provide the best performance in terms of sensitivity and efficiency in nitrate reduction. The microflower structure enhances catalytic activity in the electroreduction of nitrate, which occurs predominantly at the tips of the well-defined Cu crystals structures. These tips serve as active sites due to the presence of more exposed copper atoms at the crystal edges compared to curved surfaces. These atoms, being less coordinated, are more reactive and therefore interact more readily with $NO_3^-$. As a result, the tips facilitate local nitrate ion diffusion, reducing the mass-transport limitations typical of rounder surfaces where reactants transport surface is less effective.

Using the Randles–Ševčík equation (Eq. 5, where the number of electrons of the reaction is 2 for $NO_3^-$, and the diffusion coefficient of the redox species is $2.0 \times 10^{-6}$ $cm^2/s$ for $NO_3^-$) [21-23], the relative surface areas of the six different electrodes were calculated (Table 1).

$$i_p = (2.99 \times 10^5) * \mathrm{n}[\alpha n_a^{\frac{1}{2}}] A D_0^{\frac{1}{2}} \mathrm{C} v^{\frac{1}{2}} \quad (5)$$

A significant increase in surface area was seen for different copper-modified electrodes compared to the bare SPCE (100%). Figure 10 shows that the

calculated sensitivity for each electrode correlates with the corresponding calculated surface area.

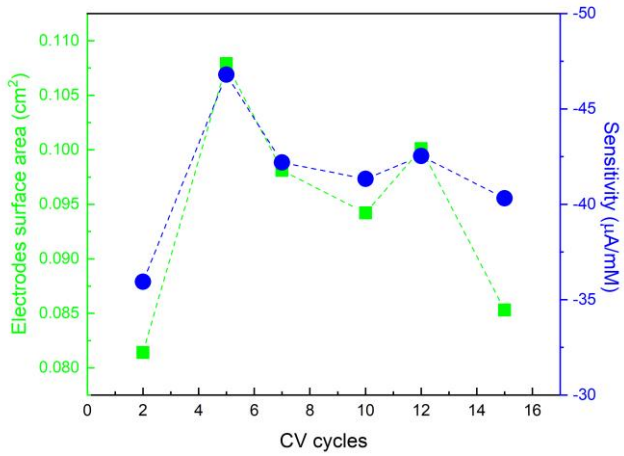


Figure 10. Sensitivity (blue dots, right vertical right) and calculated electrode surface area (green squares, left vertical axis) for 3 mM $NO_3^-$, as a function of Cu functionalization cycles.

The results confirmed that the electrode modified by 5 electrodeposition cycles is the most efficient in $NO_3^-$ reduction among the six. It is followed by the electrodes modified with 12, 7, 10, and 15 cycles, and finally the 2 cycles electrode. The differences in sensitivity and surface area can be attributed to the morphological structure of the deposited copper and the carbon coating on the electrode. A higher surface area value indicates a more active surface formed by well-defined structures, suggesting controlled growth of copper with enhanced reactivity. The presence of nucleation centers on previously formed crystals indicates more complex growth dynamics, with new copper layers forming over the existing ones (e.g., electrodes with 7 and 12 CV cycles). This is consistent with a structure that increases the active area, though not as much as the more defined microstructures from less cycles (2 and 5 CV cycles). In contrast, the formation of large, ill-defined clusters leads to a decrease in the active area, as the aggregation reduces

the surface available for nitrate reduction. Thus, the reduction in the active area is consistent with the formation of coarser and less electrochemically efficient structures (e.g., electrodes with 10 and 15 CV cycles) and a decrease in sensitivity and performances. Finally, the electrode modified with 2 CV cycles exhibits the lowest sensitivity and smallest surface area: despite the presence of copper grains with defined morphology, the electrode coverage is poor.

## 6- Study of the electrochemical reaction on electrode

The reaction mechanism was investigated by studying the electrochemical reduction of nitrate on the Cu/C electrode modified after 5 CV cycles. The Cu d-orbitals are energetically aligned with the lowest unoccupied molecular $\pi^*$ orbitals of $NO_3^-$, which facilitates efficient electron transfer at the catalyst surface [17, 24]. The scan rate effect on the $NO_3^-$ reduction peak across a range of 50 to 500 $mV \cdot s^{-1}$ allows for evaluating the reaction kinetics. As shown in Figure 11a, the peak potential (Ep) shifts toward more negative values with increasing scan rate, which is characteristic of a diffusion-controlled and electrochemically irreversible process. Figure 11b illustrates the relationship between the cathodic peak current and the square root of the scan rate. The linear increase in peak current with $\sqrt{v}$ confirms that the reduction process is controlled by diffusion, consistent with the Randles–Ševčík equation (Eq. 5).

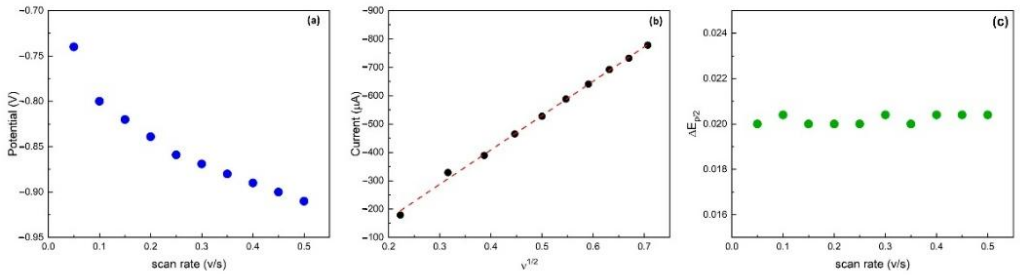


Figure 11. (a) $NO_3^-$ reduction peak potential as a function of the scan rate. (b) Maximum peak current as a function of the square root of the scan rate. The dashed red line is a linear best fit to the data. (c) $\Delta E_{p/2}$ as a function of the scan rate for nitrate reduction.

Further insight into the reaction kinetics was obtained by analyzing the half-peak potential (Ep/2), which is the potential at which the current reaches half of its maximum value. Figure 11c presents ΔEp/2 (defined as Ep – Ep/2) plotted against the scan rate. Across the scan rate range studied (50 to 500 $mVs^{-1}$), ΔEp/2 remained constant, with an average value of 20 mV (standard deviation: 2 mV, n = 3). This stability demonstrates that the transfer coefficient of the $NO_3^-$ reduction reaction is independent of the scan rate, supporting a diffusion-limited mechanism with minimal kinetic dependence on scan rate.

## 7- Electrochemical Sensor Performance for Nitrate Ion Detection in water and interferences tests

To evaluate the analytical performance of the electrochemical sensor for the detection of $NO_3^-$, linear sweep voltammetry was employed in a 0.1 M KCl electrolyte solution (pH = 7).

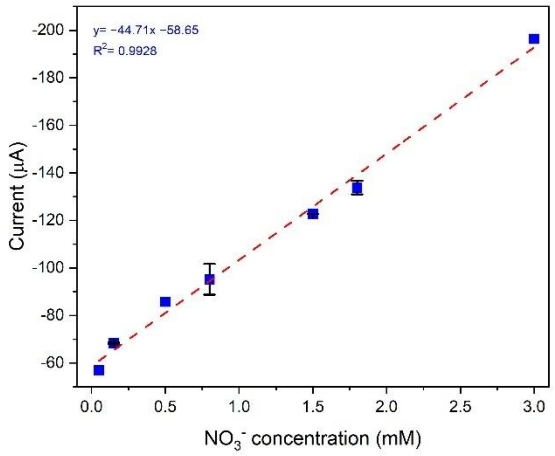


Figure 12. Calibration curve of the electrode as a function of nitrate concentration (from 0.05 to 3 mM). The points, representing the average peak current measured by three sensors, indicate the cathodic current peak maximum at – 0.86 V. The error bars account for the standard deviation (SD).

This electrolyte was selected as it provides a stable environment that enables direct measurement of $NO_3^-$ without compromising the sensor performance or requiring pH adjustment. The calibration curve was constructed by averaging three measurements of the $NO_3^-$ reduction peak current, recorded at – 0.86 V, over a concentration range of 0.05 – 3.0 mM. The resulting data showed a linear response with a sensitivity of 44.71 $\mu AmM^{-1}$, determined as the fit slope, and a coefficient of determination ($R^2$) of 0.9928 (n = 3), as reported in Figure 12. The limits of detection (LoD) were calculated using the standard formula (Eq. 6):

$$LoD = \frac{3\sigma}{s} \qquad (6)$$

where σ represents the standard deviation of the blank signal and S is the slope of the calibration curve. The LoD was estimated to be 0.87 μM. The linear increase in Cu(II) reduction peak current observed with rising nitrate concentration

highlights the catalytic role of copper in the reduction process. This catalytic behavior is consistent with findings reported by Filimonov et al. [25], who demonstrated that cuprous ions facilitate nitrate reduction due to their electrochemical activity, thus enhancing both mass transport and electron transfer at the electrode surface.

To validate the performance of the electrochemical sensor, the results were compared with those obtained using UV–vis spectrophotometry in the same nitrate concentration range and the results are summarized in Figure 13.

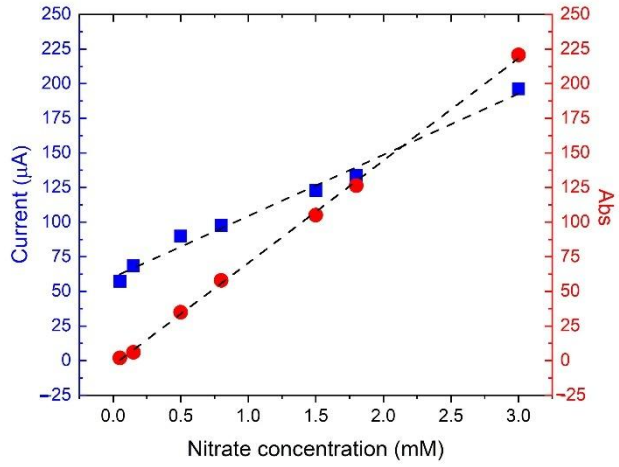


Figure 13. Calibration curve for nitrate detection using UV-vis spectrophotometer (red dots referencing the right axis) and the Cu/C sensor (blue squares referencing the left vertical axis). Each point represents the average peak current from three measurements.

Red dots (right y-axis) represent the absorbance data, while blue squares (left y-axis) represent the average peak currents from the electrochemical measurements. The comparison revealed that the electrochemical sensor sensitivity is only 1.6 times lower than the spectrophotometric method one, confirming the reliability and good analytical performance of the developed sensor.

The Cu/C-modified electrode is selective for nitrate also in the presence of common interferents. The CV curves presented in Figure 14 provide strong evidence for the selectivity of the Cu/C-modified electrode toward nitrate in the presence of typical interferents such as nitrite ($NO_2^-$) and ammonium ($NH_4^+$).

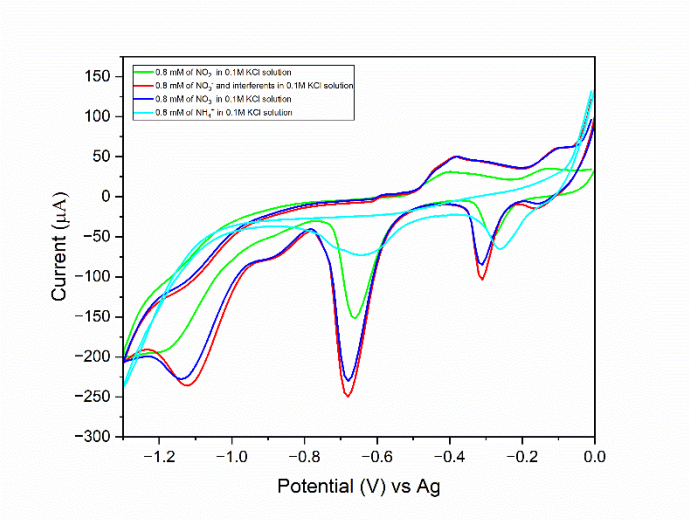


Figure 14. CV curves of the Cu/C-modified electrode in 0.1 M KCl solution containing 0.8 mM of individual nitrogen species and their mixture: nitrate (blue line), nitrite (green line), ammonium (cyan line), and a mixture of $NO_3^-$ with all interferents (red line).

As shown, the blue line corresponding to 0.8 mM $NO_3^-$ in 0.1 M KCl displays a well-defined cathodic peak at −0.86 V vs. Ag, which is the operational reduction potential for nitrate on this electrode. In contrast, the voltammograms for $NO_2^-$ (green line), and $NH_4^+$ (cyan line), at the same concentration, exhibit no significant cathodic peak at this potential, confirming the absence of electrochemical reduction processes for these species under the same conditions. This result directly demonstrates that the Cu/C-modified electrode is highly selective for nitrate, as the reduction current at −0.86 V is exclusively attributable to $NO_3^-$, with negligible contributions from potential interferents. This is due to the electrocatalytic properties of the copper based micro-crystals formed on the

carbon substrate. Copper surfaces are known to facilitate the multi-electron reduction of nitrate via the adsorption and activation of $NO_3^-$ intermediates, a process that is energetically and kinetically favoured on Cu compared to other nitrogenous species [25, 26]. Nitrite, although structurally similar, requires a different potential window for electrochemical transformation, typically at more positive potentials, and does not undergo reduction at −0.86 V. Ammonium, on the other hand, is electrochemically inert in this potential range and does not participate in redox processes on the Cu/C surface [3]. The absence of overlapping peaks or significant current responses for these interferents, even when present at the same concentration as nitrate, underscores the role of adsorption energetics and surface specificity in the observed selectivity [17]. An additional source of interference in the measurement could arise when tap water is used as the solvent, as is typical in real environmental conditions. To evaluate whether potential interferents present as impurities in tap water could affect sensor performance, two calibration curves were constructed: one using Milli-Q and the other using tap water as the solvent medium in the same $NO_3^-$ concentration range (Figure 15). The calibration points and linear fit obtained in Milli-Q water are represented as blue dots and dashed red line, respectively. In contrast, the calibration points obtained from tap water samples are shown as green squares. The first data point for tap water was validated through two independent measurements: one using the developed electrochemical sensor and the other via spectrophotometric analysis. Both methods yielded consistent results of 0.1 mM $NO_3^-$, confirming that the sensor's response is not influenced by impurities present in tap water. These findings demonstrate the robustness and selectivity of the device for nitrate detection in real water samples.

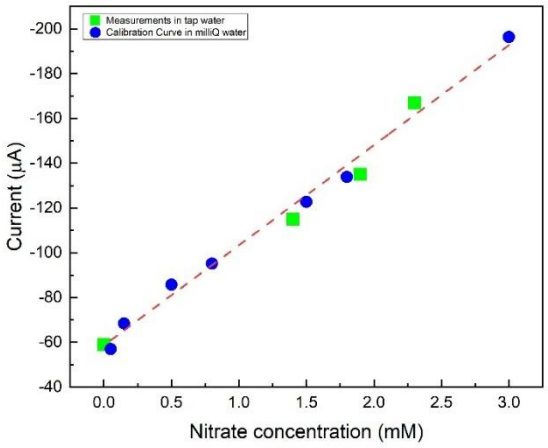


Figure 15. Calibration curves for $NO_3^-$ concentration added to MilliQ water (blue dots) and to tap water (green squares).

## 8- Application in Ammonia Production

The sensor was used in another study (N. Marino et al.) to perform quantitative measurements on an electrolytic solution for ammonia production in which nitrate, ammonium ions, and other reduced nitrogen species (such as $NH_2OH$ and $N_2H_4$) were present [27]. The device was calibrated in 0.01 M PBS solution (pH 7) for a nitrate concentration ranging from 0.25 mM to 9 mM. The PBS concentration used is the same as that used for chronoamperometric ammonia production; thus, calibration and measurements are performed on the same solution. The corresponding calibration curve, exhibiting a linear dynamic range, is shown in Figure 16.

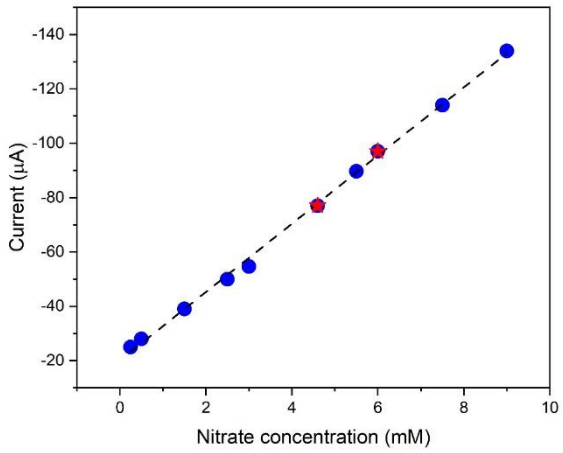


Figure 16. Calibration curves (blue dots and dashed red line) for $NO_3^-$ concentration in 0.01 M PBS electrolyte solution (pH 7) in a range from 0.25 mM to 9 mM. A linear trend is observed. Experimental points before and after ammonia production indicate an initial value of 6 mM and a final value of 4.6 mM (red stars).

The experimental data collected before and after the chronoamperometric process indicated a decrease in nitrate concentration, from an initial value of 6 mM to 4.6 mM (red stars in the figure), after ammonia production. The nitrite detection results matched the calibration curve obtained in PBS ($R^2$ = 0.997), confirming the sensor's accuracy even in complex matrices.

### 1- Reproducibility and Repeatability tests of the Sensor

The reproducibility and repeatability of the sensor measurements were evaluated. Reproducibility refers to the consistency of sensor responses when measurements are performed using different electrodes fabricated under the same conditions. Repeatability refers to the consistency of measurements obtained using the same electrode over multiple trials, reflecting the sensor's stability and performance

over time. Both aspects are critical because reproducibility ensures that the sensor fabrication process is reliable, while repeatability indicates the sensor's operational stability during use. Reproducibility was assessed by measuring seven different nitrate concentrations (0.05, 0.15, 0.5, 0.8, 1.5, 1.8, and 3.0 mM) using three independently prepared electrodes (Figure 12). Each concentration was measured in triplicate, and the RSDs calculated confirmed the high reproducibility of the sensor response. These results demonstrate the reliability and consistency of the electrode functionalization procedure.

| **Concentration (mM)** | **RDS (%) calculated on 3 measurements** |
|---|---|
| 0.05 | 0.15% |
| 0.15 | 0.39% |
| 0.5 | 0.00% |
| 0.8 | 4.89% |
| 1.5 | 0.02% |
| 1.8 | 2.83% |
| 3 | 0.00% |

Table 2. RSD values obtained for reproducibility measurements

Repeatability was evaluated by performing ten consecutive measurements of a 0.8 mM $NO_3^-$ solution using the same electrode. This concentration was chosen as it corresponds to the maximum limit set by the WHO and European directives for nitrate in drinking water.

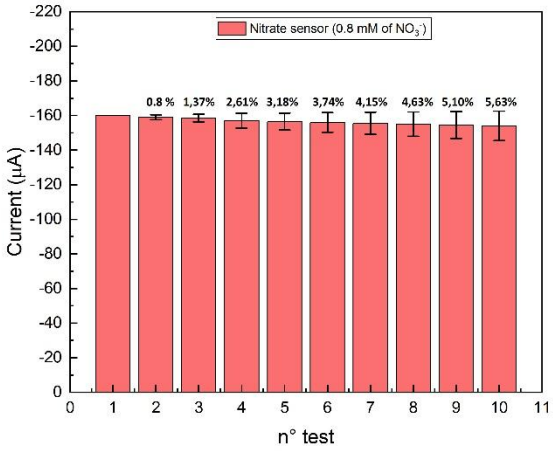


Figure 14. Repeatability test for Cu/C sensor. The reduction peak current of $NO_3^-$ was acquired from the same sample by repeating the measurement three times. The percentage reported in the figure is the difference between successive measurements and the first one.

The RSD was calculated by comparing the cathodic peak current of each measurement with that of the first one. The sensor maintained stable performance up to the tenth measurement, showing only a 5% decrease in peak current relative to the initial value, which indicates consistent performance over multiple uses (Figure 14).

| | **Tests in a 0.8 mM $NO_3^-$ solution** | | | | | | | | | |
|---|---|---|---|---|---|---|---|---|---|---|
| **RSD %** | 1 | 2 | 3 | 4 | 5 | 6 | 7 | 8 | 9 | 10 |
| | - | 0.80% | 1.37% | 2.61% | 3.18% | 3.74% | 4.15% | 4.63% | 5.10% | 5.63% |

Table 3. RSD values obtained for repeatability measurements.

This suggests that while the sensor can be reused, its operational life is limited to a certain number of repeated uses before performance degrades noticeably. Overall, the sensor demonstrated excellent reproducibility and good repeatability.

Although SPEs are generally designed for single-use applications, the sensor exhibited consistent performance over multiple measurement cycles, highlighting its potential for short-term reusability, a beneficial feature in contexts requiring repeated analyses without frequent electrode replacement.

To ensure sensor preservation, the electrodes were stored at room temperature in a dry and dark environment when not in use. Prior to each measurement, electrodes were rinsed with deionized water to eliminate residual analyte and gently dried using an inert gas stream. No additional regeneration procedures were employed, which may partially explain the gradual signal decrease observed over successive measurements.

## 2- Comparison with Literature and Discussion of Results

The nitrate detection performance observed with our sensor appears promising in comparison with recent studies based on the development of SPE-based electrochemical sensors for $NO_3^-$ detection (Table 2) [1, 3, 28, 29]. The Cu micro-flower modified SPCE developed in this work represents an advancement in the electrochemical detection of nitrate ions in aqueous environments, positioning it as a highly competitive platform compared to reported sensors. The sensor achieves a LoD of 0.87 μM, which is lower than that of many other SPE-based nitrate sensors, such as those employing gold electrodes modified with silver nanoparticles (LoD 7.7 μM) or unmodified graphite SPEs (LoD 5.0 μM) [29, 30]. Although the Cu nanocluster-modified Ag SPE achieves exceptional sensitivity with a sub-nanomolar LoD, its limited linear range restricts its applicability in scenarios where high nitrate concentrations are present [3]. Conversely, SWCNT-modified Cu and Pd–Cu electrodes offer an extended linear range but suffer from

higher detection limits, making them more suitable for environmental monitoring at moderate nitrate levels [1].

| Electrode | LoD | Linear Range | Application | Reference |
|---|---|---|---|---|
| SPE modified with Cu micro-flowers (This work) | 0.87 µM | 0.05-3.0 mM | Drinking water, tap water | This work |
| AuSPE/AgNPs (Ag nanoparticles on Au SPE) | 7.7 µM | 0.1-1.5 mM | Freshwater, tap water | [28] |
| Graphite SPE | 5.0 µM | 10–500 µM | On-site detection in aqueous samples; Aquaponic pond | [29] |
| SPE modified with SWCNT-modified Cu and Pd-Cu | 52 µM | 0.1–7.8 mM | Environmental water analysis | [1] |
| AgSPE modified with Cu nanoclusters | 0.207 µM | 50-500 µM | Drinking water | [3] |

Table 2. Comparison of this work with some of the literature electrochemical sensing platforms for nitrate detection.

The Cu micro-flower modified carbon SPE developed here strikes a balance between sensitivity and dynamic range, combining a low LoD with a broad linear range. This makes the sensor attractive for routine water quality monitoring, where both trace and elevated nitrate levels may be encountered in diverse samples.

An additional strength of this sensor lies in its simplicity and cost-effectiveness. The copper micro-flower structures are fabricated via cyclic voltammetric deposition directly onto commercial carbon SPEs, eliminating the need for complex synthesis protocols or expensive nanomaterials. This renders the approach scalable, reproducible, and ideal for on-site field deployment, aligning with current demands for decentralized, low-cost analytical technologies in environmental sensing.

## CONCLUSION

The nitrate sensor (Cu/C) achieved a high sensitivity of 44.71 μA/μM, a remarkably low LoD of 0.87 μM, and a linear range of 0.05–3 mM, meeting and exceeding the stringent requirements set by WHO and EU regulations for drinking water quality. Key to the sensor's performance is the flower-like structure of the crystallites, generated after 5 cycles of CV that favors a greater catalytic effect. The sensor showed insignificant interference from common water contaminants, independence from the electrochemical medium used (KCl and PBS were employed), high reproducibility (maximum RSD 4.89%), and good repeatability, although the progressive decrease in signal intensity upon repeated measurements indicates the need for further optimization of its operational stability.

REFERENCES

[1] Chiydem Hyusein, V.; Tsakova, V. Nitrate detection at Pd-Cu-modified carbon screen printed electrodes. *J. Electroanal. Chem.* **2023**, *930*, 117172. https://doi.org/10.1016/j.jelechem.2023.117172.

[2] Dima, G. E.; De Vooys, A. C. A.; Koper, M. T. M. Electrocatalytic reduction of nitrate at low concentration on coinage and transition-metal electrodes in acid solutions. *J. Electroanal. Chem.* **2003**, *554–555*, 15–23. https://doi.org/10.1016/s0022-0728(02)01443-2.

[3] Inam, A. K. M. S.; Costa Angeli, M. A.; Shkodra, B.; Douaki, A.; Avancini, E.; Magagnin, L.; Petti, L.; Lugli, P. Flexible Screen-Printed Electrochemical Sensors Functionalized with Electrodeposited Copper for Nitrate Detection in Water. *ACS Omega* **2021**, *6*, 33523–33532. https://doi.org/10.1021/acsomega.1c04296.

[4] Chen, G.; Li, N.; Luo, Y.; Wang, Y.; Wang, G. Recent Advances in Copper-Based Electrocatalysts for Nitrate Reduction. *ChemElectroChem* **2023**, *10*, e202200833. https://doi.org/10.1002/celc.202200833.

[5] Wang, Y.; Zhang, Y.; Liu, S.; Wang, X.; Liu, Y. Copper-Based Nanostructured Catalysts for Efficient and Selective Electrochemical Nitrate Reduction. *ACS Appl. Mater. Interfaces* **2022**, *14*, 12345–12353. https://doi.org/10.1021/acsami.2c01234.

[6] Wang, Z.; Wang, Y.; Zhang, Y.; Liu, S.; Zhang, L. Copper Microflowers and Their Oxides for Efficient Electrocatalytic Nitrate Reduction. *J. Electroanal. Chem.* **2023**, *928*, 117100. https://doi.org/10.1016/j.jelechem.2023.117100.

[7] Zhang, Y.; Wang, Y.; Liu, S.; Wang, X.; Zhang, L.; Liu, Y. Flower-like Copper Microstructures as Efficient Electrocatalysts for Nitrate Reduction. *Electrochim. Acta* **2021**, *388*, 138635. https://doi.org/10.1016/j.electacta.2021.138635.

[8] Liu, S.; Wang, Y.; Wang, X.; Zhang, L.; Liu, Y. Enhanced Electrocatalytic Nitrate Reduction on Copper Oxide Nanostructures: Role of Surface Defects and Morphology. *J. Mater. Chem. A* **2022**, *10*, 11449–11458. https://doi.org/10.1039/D2TA01944K.

[9] Li, J.; Wang, Z.; Zhang, X.; Yu, Y.; Wang, Y. Design of Defect-Rich Copper Oxide Nanostructures for Enhanced Nitrate Reduction. *J. Mater. Chem. A* **2021**, *9*, 17045–17054. https://doi.org/10.1039/D1TA03381A.

[10] Farina, R.; D'Arrigo, G.; Alberti, A.; Capuano, G. E.; Corso, D.; Screpis, G. A.; Coniglio, M. A.; Condorelli, G. G.; Libertino, S. Electrochemical Growth of Copper Crystals on SPCE for Electrocatalysis Nitrate Reduction. *Nanomaterials* **2024**, *14*, 1704. https://doi.org/10.3390/nano14211704.

[11] Farina, R.; D'Arrigo, G.; Alberti, A.; Scalese, S.; Capuano, G. E.; Corso, D.; Screpis, G. A.; Coniglio, M. A.; Condorelli, G. G.; Libertino, S. Copper Micro-Flowers for Electrocatalytic Sensing of Nitrate Ions in Water. *Sensors* **2024**, *24*, 4501. https://doi.org/10.3390/s24144501.

[12] Yao, Y.; Zhang, L. Electrochemical nitrate reduction to ammonia on copper-based materials for nitrate-containing wastewater treatment. *Sci. Bull.* **2022**, *67*, 1194–1196.

[13] Li, C.; Liu, S.; Xu, Y.; Ren, T.; Guo, Y.; Wang, Z.; Li, X.; Wang, L.; Wang, H. Controllable reconstruction of copper nanowires into nanotubes for efficient electrocatalytic nitrate conversion into ammonia. *Nanoscale* **2022**, *14*, 12332–12338. https://doi.org/10.1039/D2NR02647B.

[14] Xu, Y.; Wang, M.; Ren, K.; Ren, T.; Liu, M.; Wang, Z.; Li, X.; Wang, L.; Wang, H. Atomic defects in pothole-rich two-dimensional copper nanoplates triggering enhanced electrocatalytic selective nitrate-to-ammonia transformation. *J. Mater. Chem. A* **2021**, *9*, 16411–16417. https://doi.org/10.1039/D1TA03569B.

[15] Li, J.; Yang, H.; Wu, S. Influence of crystallographic orientation on the electrocatalytic reduction of nitrate by copper electrodes. *ACS Catal.* **2018**, *8*, 2735–2744. https://doi.org/10.1021/acscatal.7b04466.

[16] Patil, S. B.; Liu, T.-R.; Chou, H.-L.; Huang, Y.-B.; Chang, C.-C.; Chen, Y.-C.; Lin, Y.-S.; Li, H.; Lee, Y.-C.; Chang, Y. J.; et al. Electrocatalytic Reduction of NO3− to Ultrapure Ammonia on {200} Facet Dominant Cu Nanodendrites with High Conversion Faradaic Efficiency. *J. Phys. Chem. Lett.* **2021**, *12*, 8121–8128.

[17] Zhang, R.; Zhang, S.; Cui, H.; Guo, Y.; Li, N.; Zhi, C. Electrochemical nitrate reduction to ammonia using copper-based electrocatalysts. *Next Energy* **2024**, *4*, 100125.

[18] Chen, D.-J.; Lu, Y.-H.; Wang, A.-J.; Feng, J.-J.; Huo, T.-T.; Dong, W.-J. Facile synthesis of ultra-long Cu microdendrites for the electrochemical detection of glucose. *J. Solid State Electrochem.* **2012**, *16*, 1313–1321.

[19] Mumtarin, Z.; Rahman, M. M.; Marwani, H. M.; Hasnat, M. A. Electro-kinetics of conversion of NO3− into NO2− and sensing of nitrate ions via reduction reactions at copper immobilized platinum surface in the neutral medium. *Electrochim. Acta* **2020**, *346*, 135994. https://doi.org/10.1016/j.electacta.2020.135994.

[20] Zadeh Zhad, L. H. R.; Lai, R. Y. Comparison of nanostructured silver-modified silver and carbon ultramicroelectrodes for electrochemical detection of nitrate. *Anal. Chim. Acta* **2015**, *892*, 153–159. https://doi.org/10.1016/j.aca.2015.07.031.

[21] González-Meza, O. A.; Larios-Durán, E. R.; Gutiérrez-Becerra, A.; Casillas, N.; Escalante, J. I.; Bárcena-Soto, M. Development of a Randles-Ševčík-like equation to

predict the peak current of cyclic voltammetry for solid metal hexacyanoferrates. *J. Solid State Electrochem.* **2019**, *23*, 3123–3133.

[22] Elgrishi, N.; Rountree, K. J.; McCarthy, B. D.; Rountree, E. S.; Eisenhart, T. T.; Dempsey, J. L. A Practical Beginner's Guide to Cyclic Voltammetry. *J. Chem. Educ.* **2018**, *95*, 197–206.

[23] Abdi, Z.; Vandichel, M.; Sologubenko, A. S.; Willinger, M.-G.; Shen, J.; Allakhverdiev, S. I.; Najafpour, M. M. The importance of identifying the true catalyst when using Randles-Sevcik equation to calculate turnover frequency. *Int. J. Hydrogen Energy* **2021**, *46*, 37774–37781.

[24] Zhao, Y.; Liu, Y.; Zhang, Z.; Mo, Z.; Wang, C.; Gao, S. Flower-like open-structured polycrystalline copper with synergistic multi-crystal plane for efficient electrocatalytic reduction of nitrate to ammonia. *Nano Energy* **2022**, *97*, 107124.

[25] Filimonov, E. V.; Shcherbakov, A. I. Catalytic Effect of Copper Ions on Nitrate Reduction. *Prot. Met.* **2004**, *40*, 280–285.

[26] Bai, L.; Franco, F.; Timoshenko, J.; Rettenmaier, C.; Scholten, F.; Jeon, H. S.; Yoon, A.; Rüscher, M.; Herzog, A.; Haase, F. T.; Kühl, S.; Chee, S. W.; Bergmann, A.; Cuenya, B. R. [Full title]. *J. Am. Chem. Soc.* **2024**, *146*, 9665–9678. https://doi.org/10.1021/jacs.3c13288.

[27] Marino, N.; Milazzo, R. G.; Farina, R.; Bongiorno, C.; Libertino, S.; Lombardo, S. A.; Privitera, S. M. S. High Performance Fe-MoS2 Electrocatalyst for Efficient Nitrate Reduction to Ammonia: Synergistic Design for Sustainable Ammonia Production. *ACS Sustain. Chem. Eng.* DOI pending.

[28] Ben Messaoud, N.; dos Santos, M. B.; Espiña, B.; Queirós, R. B. Development of electrochemical sensors based on silver nanoparticles electrodeposited on gold screen-printed electrodes: application to nitrate trace analysis in water. *J. Sens. Sens. Syst.* **2024**, *13*, 135–145. https://doi.org/10.5194/jsss-13-135-2024.

[29] Concepcion, R.; Duarte, B.; Palconit, M. G.; Baun, J. J.; Bandala, A.; Vicerra, R. R.; Dadios, E. Screen-printed graphite electrode on polyvinyl chloride and parchment strips integrated with genetic programming for in situ nitrate sensing of aquaponic pond water. *Information Processing in Agriculture* **2024**, *11*, 187–201. https://doi.org/10.1016/j.inpa.2023.02.002.

# CHAPTER 3

# NITRITE ION SENSING

## 1- Introduction and State of the Arts

Nitrites are intermediate nitrogen species in the nitrogen cycle. Although less stable than nitrates, they play a key role in environmental redox processes. Their presence in water often indicates disruptions in nitrification or denitrification processes and may also result from industrial discharges or untreated wastewater. Even at low concentrations, nitrites pose significant health concerns due to their ability to form carcinogenic nitrosamines and induce methemoglobinemia [1]. Accurate and selective detection of nitrites is therefore critical for water quality assessment. Several studies have demonstrated the potential of modified SPEs for nitrite detection, utilizing different electrode surface modifications. Adiraju et al. developed an electrochemical sensor based on carbon SPE modified with Au NPs for nitrite detection in groundwater, achieving a LoD of 0.38 μM [2]. The principle of operation is the electrochemical oxidation of $NO_2^-$ at pH 6.5 in PBS buffer during a square wave voltametric (SWV) scan. Rajab et al. developed an electrochemical sensor based on a SPE modified with zirconia nanoparticles and multi-walled carbon nanotubes ($ZrO_2$@MWCNTs/SPE) for selective detection of nitrite in food and water samples. The SPE modification with the composite $ZrO_2$@MWCNTs resulted in an enhanced peak current of nitrite compared to the bare electrode signal, thanks to the enhanced electron transfer rate. This is attributed to the combination of the tubular shape of MWCNTs and the crystallinity of $ZrO_2$, providing abundant electron transport pathways and active sites, which improve nitrite absorption during the oxidation reaction. The main electrochemical reaction involved in the detection process is the oxidation of nitrite to nitrate ions. The device showed a LoD of 0.94 μM, with high sensitivity and selectivity [3].

This chapter presents the development of an SPE-based electrochemical sensor for $NO_2^-$ detection in water.

## 2- Materials and Methods

The nitrite sensor was manufactured starting from a screen-printed electrode, comprising a silver reference electrode, a carbon counter electrode, and a carbon working electrode modified by electrodeposition of copper and manganese oxides. The carbon electrode, chosen for its electrochemical stability and conductivity, provides an ideal substrate for the deposition of copper and manganese, further improving the process efficiency [2,3]. The choice of combining CuO and $MnO_2$ for nitrite detection is motivated by their complementarity. While CuO in previous studies has proven to be effective for $NO_2^-$ detection [4-6], and in $NO_3^-$ reduction [7,8], $MnO_2$ is widely recognized for its high activity towards nitrite oxidation. CuO and $MnO_2$ work together synergistically as efficient catalysts for the electrooxidation of nitrite to nitrate, thanks to their complementary redox properties [9]. The $MnO_2$/CuO synergy, combining $Mn^{4+}/Mn^{3+}$ redox mediation with CuO's oxygen-vacancy-enabled adsorption, effectively discriminates against non-target species while stabilizing $NO_2^-$ intermediates. Phosphate-buffered saline (PBS, pH 7) was selected as the supporting electrolyte to ensure a stable and well-controlled environment, which is essential for achieving consistent and reproducible electrochemical measurements. While PBS is widely used in biological and physiological applications, its neutral pH and effective buffering capacity also make it an appropriate medium for simulating natural water conditions, which typically exhibit near-neutral pH values. Moreover, the use of PBS in this study highlights the potential applicability of the nitrite sensor in the analysis of physiological fluids and treated water samples. Functionalization of the working electrode was carried out by cyclic voltammetry, and sensor performance was examined by linear sweep voltammetry.

### 3- Cu-Mn/C Electrode Fabrication

Electrode preparation was performed via cyclic voltammetric electrodeposition of manganese and copper oxides, according to the schematic reported in Figure 1. $MnO_2$ particles were deposited electrochemically on the mesoporous carbon WE surface (4-mm diameter) by CV in the potential range from 0.0 V to 1.2 V at a scan rate of 0.05 V $s^{-1}$ by 5 consecutive scans using 0.1 M $MnCl_2$ in 1 M KCl supporting electrolyte [10]. The electrodeposition of $MnO_2$ occurs via an anodic process, where $Mn^{2+}$ ions are oxidized to $Mn^{4+}$ under the application of anodic potentials. The overall reaction is:

$$Mn^{2+} + 2H_2O \rightarrow MnO_2 + 4H^+ + 2e^-$$

$Mn^{2+}$ ions adsorb onto the carbon surface. At moderate potentials, $Mn^{2+}$ is oxidized to the intermediate $Mn^{3+}$ and subsequently is further oxidized to $Mn^{4+}$, thus precipitating as hydrated $MnO_2$. This process explains why the XPS analyses found traces of $Mn_2O_3$ oxides.

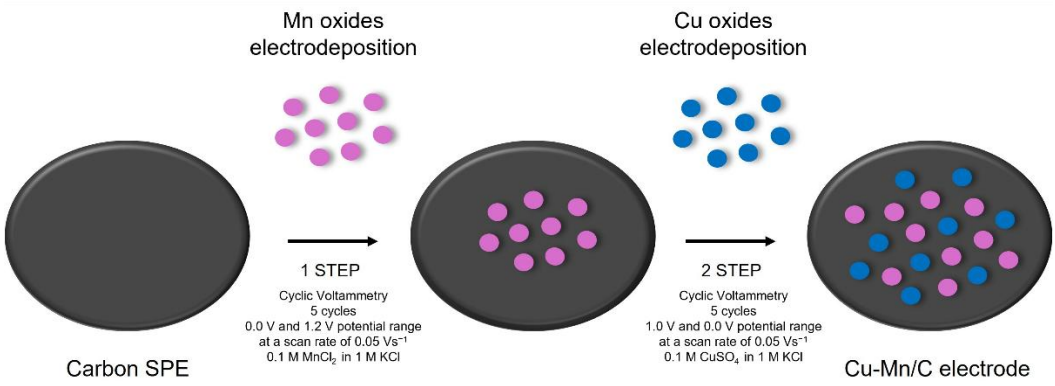


Figure 1. Schematic representation of the Cu–Mn/C electrode functionalization process.

Subsequently, Cu particles were electrodeposited via CV in the potential range from 1.0 V to 0.0 V at a scan rate of 0.05 V $s^{-1}$ by 5 consecutive scans using 0.1 M $CuSO_4 \cdot 5H_2O$ in 1 M KCl supporting electrolyte [8]. The presence of $MnO_2$ on

the electrode surface promotes the formation of CuO rather than metallic Cu because, under anodic polarization, $MnO_2$ remains stable and may even participate in redox mediation.

## 4- Morphological and compositional characterization of Cu-Mn/C electrode

Scanning electron microscopy analysis investigated the carbon substrate surface (Figure 2a) and the electro-deposited manganese and copper species morphology (Figure 2b). The unmodified carbon electrode has a relatively homogeneous surface, featuring the typical microporous texture and shallow fissures associated with screen-printed carbon materials. In contrast, the CuO-$MnO_2$ modified carbon electrode (thereafter Cu-Mn/C) presents a different surface morphology, characterized by a dense array of rod-like and needle-shaped nanocrystals (ranging from 100 to 500 nm in length) unevenly distributed across the carbon surface.

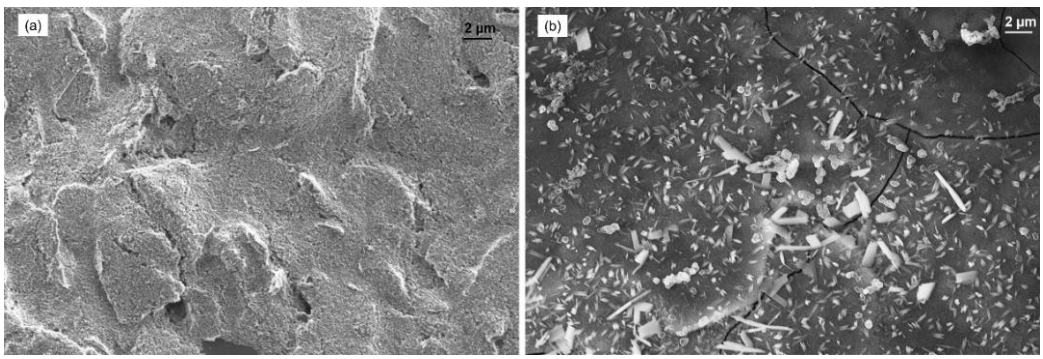


Figure 2. SEM images of: (a) carbon bare electrode surface, (b) Cu-Mn/C modified electrode surface.

Energy-Dispersive X-ray (EDX) spectroscopy (Figure 3) confirms the co-deposition of copper and manganese, with quantitative analysis indicating a

higher copper content (45.20 wt%) than manganese (4.29 wt%). The substantial oxygen presence (29.39 wt%) suggests the formation of metal oxides rather than pure metals, while the residual chlorine content (9.19 wt%) likely results from the KCl electrolyte. Elemental mapping demonstrates the spatial distribution of copper, manganese, and carbon on the electrode surface. The Cu L map shows a highly uniform and dense coverage of copper containing species, suggesting homogeneous CuO distribution. The Mn K map reveals manganese well-dispersed throughout the surface, though less densely than copper. Magenta spots indicate $MnO_2$ presence, confirming it is effectively deposited and accessible for electrocatalytic reactions. The C K map shows the exposed carbon substrate, confirming its contribution to electrical conductivity and mechanical support for the metal oxide layers.

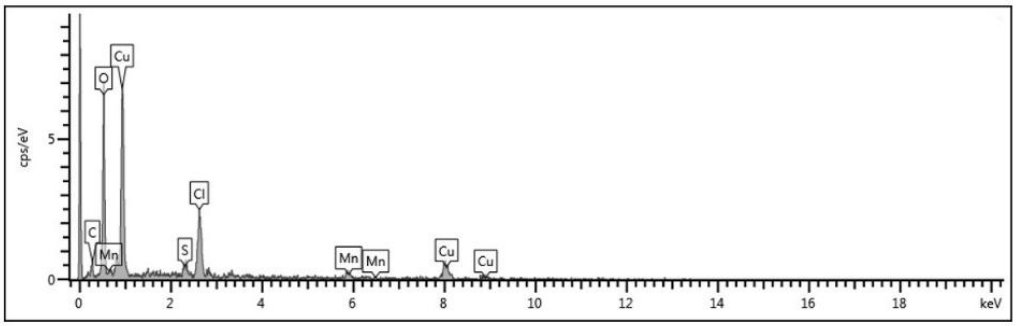


| Element | Wt % | Wt% Sigma |
|---|---|---|
| C | 10.45 | 2.24 |
| O | 29.39 | 1.43 |
| S | 1.48 | 0.34 |
| Cl | 9.19 | 0.67 |
| Mn | 4.29 | 0.85 |
| Cu | 45.20 | 1.83 |
| Total: | 100.00 | |

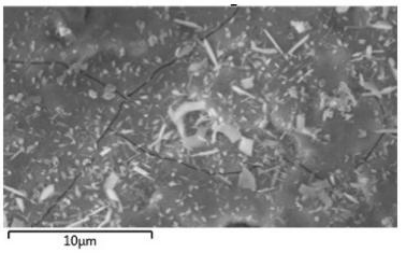

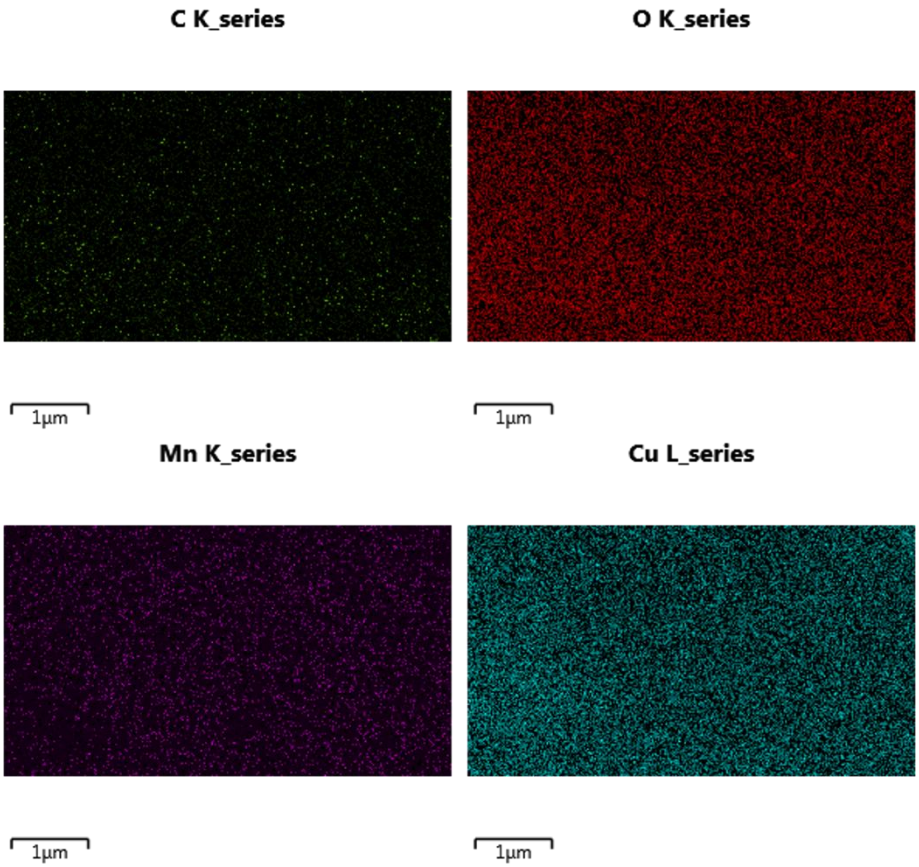


Figure 3. EDX analysis and elemental mapping of the Cu-Mn/C electrode surface.

The surface modification was further characterized using Raman and X-ray photoelectron spectroscopy (XPS). Raman analysis (Figure 4) showed distinct peaks in the 0-800 $cm^{-1}$ region. A sharp band at 150 $cm^{-1}$ was attributed to Mn-O-Mn bridging vibrations in $MnO_2$ [11,12]. Peaks at 200-250 $cm^{-1}$ corresponded to overlapping modes of $Mn_3O_4$/$Mn_2O_3$ and CuO, while the broad band between 500-700 $cm^{-1}$ reflected Mn-O stretching in $MnO_2$ (570-650 $cm^{-1}$) and CuO (615 $cm^{-1}$)[12-15].

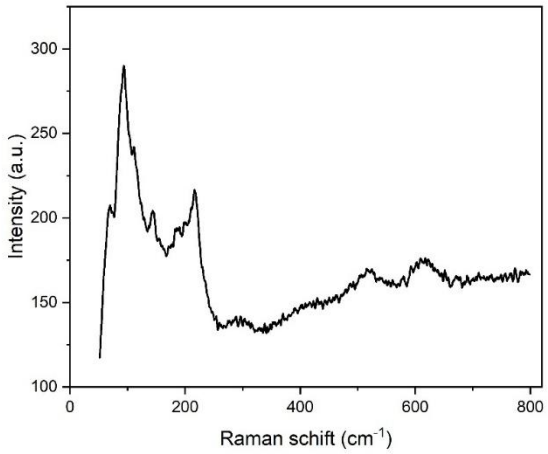


Figure 4. Raman spectra of Cu-Mn/C electrode surface.

XPS analysis supported Raman findings. The Cu 2p region exhibited a Cu $2p_{3/2}$ peak at 933 eV with its characteristic satellite at 940-945 eV, indicating the presence of CuO (Figure 5a) [16] The Mn 2p spectrum had a Mn $2p_{3/2}$ peak at 641 eV, consistent with Mn(IV) in $MnO_2$, with small shoulders suggest traces of Mn(III) (Figure 5b) [16-18]. The survey scan (Figure 5c) identified C 1s (285 eV), O 1s (530 eV) peaks, confirming a heterogeneous layer composed of $MnO_2$ and CuO, with possible minor contributions from $Mn_2O_3$ and $Cu(OH)_2$. this bifunctional oxide coating, with mixed redox-active sites validated by vibrational and electronic structure analyses, is weel-suited for electrocatalytic applications. Following nitrite detection, XPS analysis revealed a notable decrease in Cu and Mn signal intensities, compared to the pristine electrode (Figure 5d). Initial spectra of Cu and Mn confirm the presence of CuO and $MnO_2$, respectively. After sensing, the marked reduction indicated a partial reduction, dissolution, or structural modification of the metal oxides. These changes demonstrate that CuO and $MnO_2$ actively engage in nitrite electrochemical detection through redox processes, functioning as catalytic sites in line with the known behavior of transition metal oxide-based sensors.

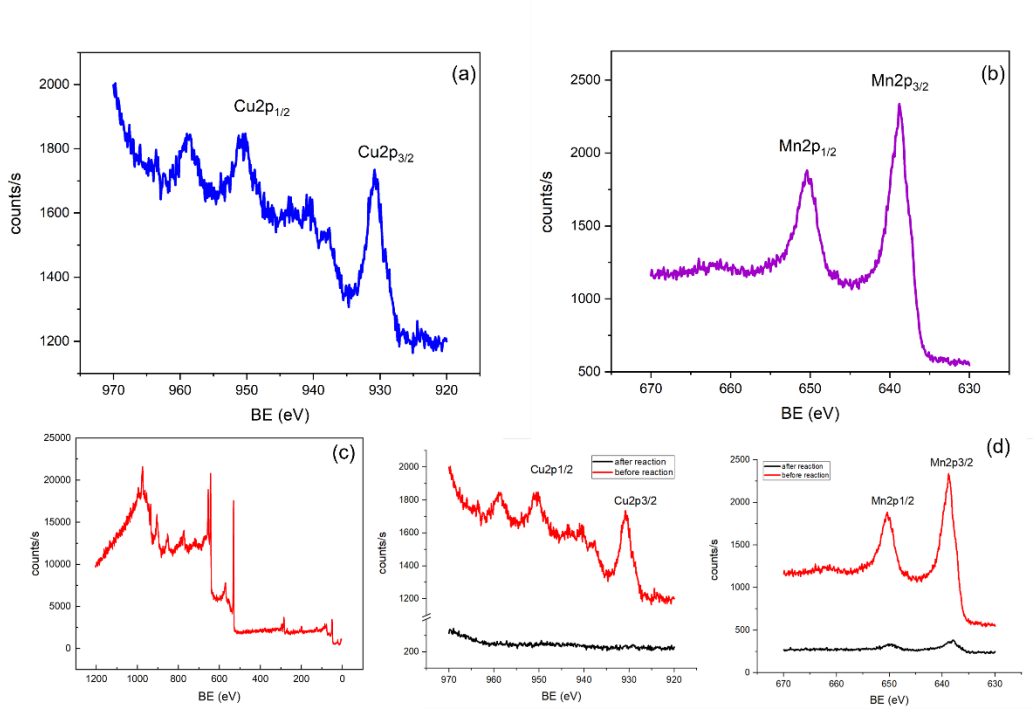


Figure 5. XPS analysis of the Cu–Mn/C electrode. (a) High-resolution Cu 2p spectrum; (b) High-resolution Mn 2p spectrum; (c) XPS survey scan; (d) Comparison of Cu 2p (left) and Mn 2p (right) spectra before (red line) and after (black line) the electrochemical reaction. The main peaks in all figures are labelled.

Although XPS and Raman spectroscopy confirmed the presence of CuO and MnO on the carbon electrode, X-ray diffraction analysis (XRD) did not detect these phases. This result indicates that the metal oxides are likely present in poorly crystalline or amorphous phases, lacking sufficient long-range order and/or being highly dispersed on the carbon surface. Therefore, the heterogeneous nature of the deposit, with crystallites of varying size and morphology, suggests the coexistence of multiple oxide phases in both crystalline and amorphous states.

## 5- Electrochemical characterization of Cu-Mn/C electrode

Electrochemical characterization of both the bare screen-printed carbon electrode (SPCE) and the Cu-Mn/C modified electrode was conducted in a 0.01 M PBS electrolyte solution, in the absence and presence of nitrite (30 µM $NO_2^-$) (Figure 6a-b). The unmodified SPCE (black line) displayed a featureless voltammogram over the investigated potential window, confirming its electrochemical inactivity toward nitrite under the tested conditions.

In contrast, the Cu-Mn/C modified electrode (red trace) exhibited distinct redox peaks: a cathodic peak ($c_1$) at −0.3 V, likely corresponding to the reduction of copper oxides (CuO to Cu), and an anodic peak ($a_1$) at +0.2 V, attributable to the re-oxidation of Cu to CuO [19,20]. The large peak-to-peak separation (ΔEp = 0.4 V) suggests an irreversible redox process. An additional anodic peak ($a_2$) at 0.0 V is assigned to the reduction of manganese oxides ($MnO_2$ to $Mn^{2+}$), while the cathodic peak ($c_2$) at −0.7 V reflects the reverse oxidation process [19-22].

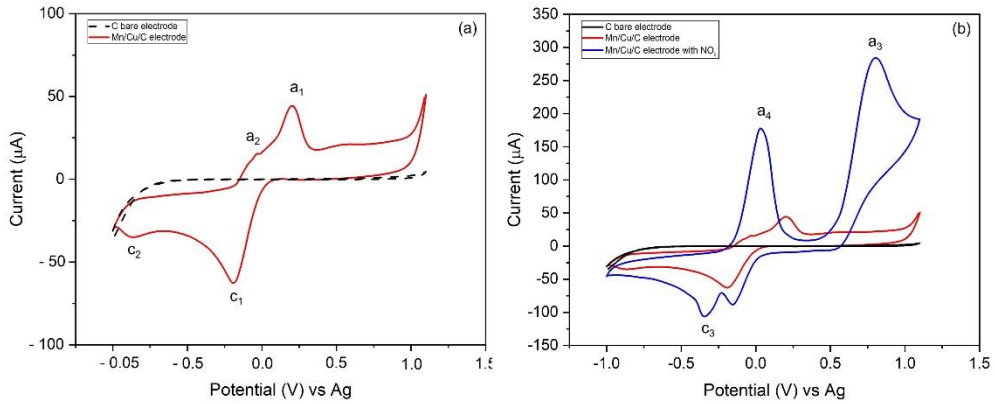


Figure 6. Cyclic voltammograms in 0.01 M PBS of: (a) bare SPCE (black trace) and Cu-Mn/C modified electrode (red trace); (b) same electrodes plus Cu-Mn/C modified electrode in the presence of 30 µM $NO_2^-$ (blue trace).

In the presence of nitrite (blue trace, Figure 6b), a new anodic peak appears around +0.8 V ($a_3$), corresponding to the electrochemical oxidation of nitrite to nitrate [22,23]. A cathodic peak at −0.4 V ($c_3$) may be associated with the reduction of nitrate to nitrite or intermediate species. Furthermore, the voltammogram shows an enhanced and negatively shifted reduction peak ($a_4$) associated with CuO and $MnO_2$, indicating that these oxides act as efficient electrocatalysts for nitrite oxidation. The observed negative shift and increased signal intensity suggest that the CuO and $MnO_2$ species on the electrode surface synergistically facilitate nitrite oxidation by lowering the activation energy barrier for its conversion to nitrate.

## 6- Electrochemical reaction at the Cu-Mn/C modified electrode

To further investigate the electrochemical oxidation mechanism of $NO_2^-$ at the Cu–Mn/C electrode, cyclic voltammetry was performed as a function of the scan rate (ranging from 50 to 350 mV/s). A linear relationship was observed between the anodic peak current (Ip) and the square root of the scan rate ($\nu^{1/2}$), indicating a diffusion-controlled process (Figure 7).

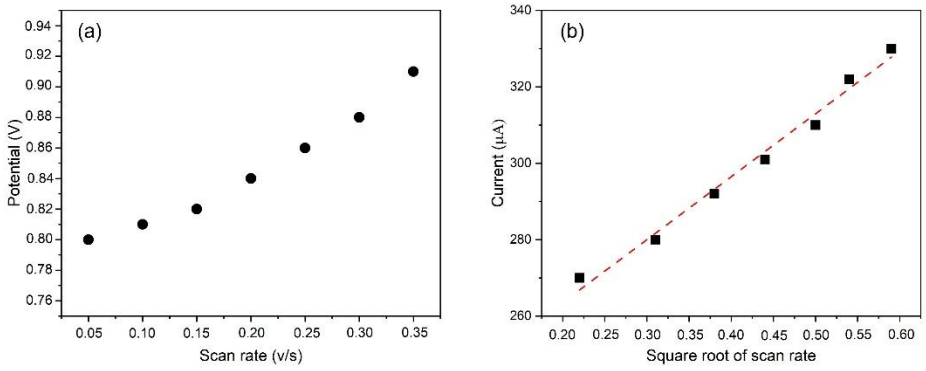


Figure 7. (a) $NO_2^-$ oxidation peak potential as a function of the scan rate. (b) Anodic peak current as a function of the square root of the scan rate; red dashed line is the data linear fit.

This behavior aligs with the Randles–Ševčík equation for irreversible systems [24]:

$$i_p = (2.99 \times 10^5) * \mathrm{n}[\alpha n_a^{\frac{1}{2}}]\, A D_0^{\frac{1}{2}}\, \mathrm{C}\nu^{\frac{1}{2}} \quad (1)$$

where $i_p$ is the peak current, $\alpha$ is the transfer coefficient, $n_a$ is the number of electrons in the rate-determining step (2 for $NO_2^-$), $A$ is the active surface area ($cm^2$), $D_o$ is the diffusion coefficient ($1.9 \times 10^{-5}$ $cm^2$ $s^{-1}$ at 25 °C), $v$ is the scan rate (V/s), and $C$ is the analyte concentration (mol $cm^{-3}$) [3].

The significant peak separation (Figure 6b) and the positive shift of the peak potential with increasing scan rates confirm that $NO_2^-$ oxidation at the Cu–Mn/C electrode is governed by an irreversible electron transfer process.

## 7- Electrochemical Sensor Performance for Nitrite Ion Detection in water and interferences tests

To evaluate its sensing performance, the Cu-Mn/C electrode was tested using linear sweep voltammetry in a 0.01 M PBS solution at pH 7 with varying $NO_2^-$ concentrations (0.2 – 60 µM). The anodic peak current at +0.8 V was used for quantification. Each data point represents the mean of three replicates, with error bars indicating the standard deviation (Figure 8). Relative standard deviation ranged from 0.04% to 6.48% indicating good reproducibility and robust electrode fabrication.

The sensor exhibited a linear response across the tested concentration range, with a sensitivity of 10.83 µA/µM and an $R^2$ value of 99.87%, with excellent linearity. The limit of detection, calculated using a signal-to-noise ratio of 3, was 0.071 µM (71 nM).

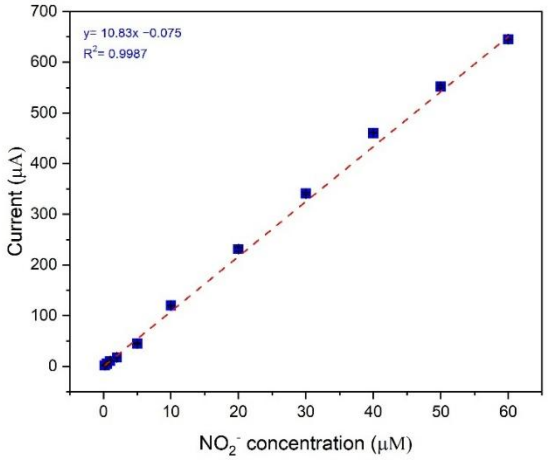


Figure 8. Calibration curve of the Cu-Mn/C electrode for $NO_2^-$ detection. Each point represents the average current at +0.8 V from three replicates. Error bars show SD.

Preliminary experiments were also performed using electrodes modified only with $MnO_2$ (Figure 9).

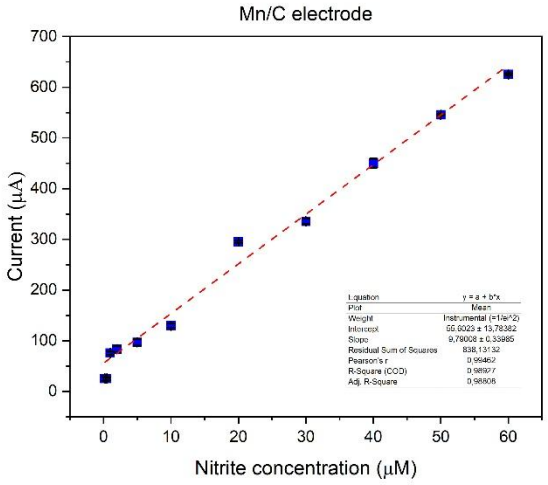


Figure 9. Calibration curve for $MnO_2$ modified (Mn/C) electrode with increasing nitrite concentration (0.2 - 60 μM).

The corresponding calibration curve, acquired in the same range above reported, revealed inferior performance, with an $R^2$ of 0.9892 and a higher LoD of 0.097 µM, confirming the enhanced sensitivity provided by the Cu incorporation. This observation further motivated the incorporation of Cu onto the Mn/C-based electrode to enhance the performance of $MnO_2$ alone. Indeed, after this modification, excellent linearity in the detection response was achieved, which enabled a significant reduction in the detectable concentration range of the nitrite ions.

The selectivity of the Cu-Mn/C-modified electrode was evaluated in the presence of common nitrogen-containing interferents, including nitrate and ammonium. Cyclic voltammetry was performed in 0.01 M PBS solution containing 30 µM of each species, both individually and as a mixture. The results, presented in Figure 10, provide strong evidence for the selectivity of the Cu/C-modified electrode toward nitrite in the presence of typical interferents.

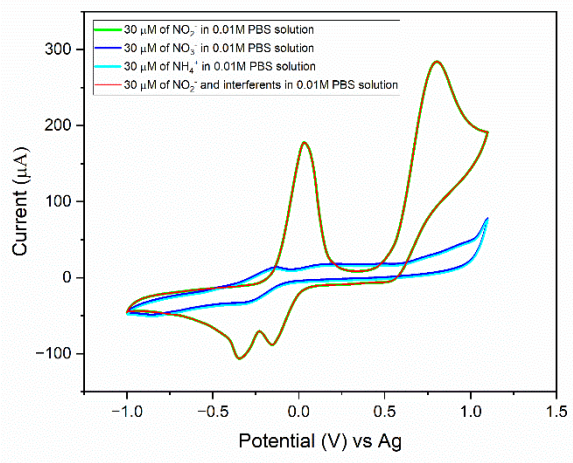


Figure 10. CV of the Cu-Mn/C-modified electrode in 0.01 M PBS solution containing 30 µM of nitrite (green line), nitrate (blue line), ammonium (green line), and their mixture (red line).

Only $NO_2^-$ produced a well-defined anodic peak at +0.8 V vs. Ag (red line), which is the operational oxidation potential for nitrite on this electrode. Neither $NO_3^-$ (blue line), nor $NH_4^+$ (green line), displayed any signal at this potential, confirming the selectivity of the electrode under the same conditions. This result demonstrates that the Cu-Mn/C modified electrode is highly selective for nitrite. Nitrate, although structurally similar, typically undergoes redox transformation at more negative potentials, while ammonium is electrochemically inert in this potential window. Thus, the reduction current at +0.8 V is exclusively attributable to $NO_2^-$, with negligible contributions from potential interferents.

## 8. Application in Ammonia Production

The sensor was also employed in a study by N. Marino et. al. [25] to quantitatively monitor nitrite in a complex electrolyte used for ammonia production, which contained nitrate, ammonium, hydroxylamine ($NH_2OH$), and hydrazine ($N_2H_4$). The sensor was calibrated in 0.01 M PBS solution (pH 7), the same used for chronoamperometric ammonia production, over a concentration range of 0.05 – 6 mM. The calibration curve, exhibiting a linear dynamic range, is shown in Figure 11. Experimental data showed an increase in nitrite concentration from 0 to 0.8 mM (red star in the figure) following the electrochemical ammonia production experiment. This value aligns with the calibration curve ($R^2 = 0.993$), confirming the accuracy and applicability of the sensor in complex matrices.

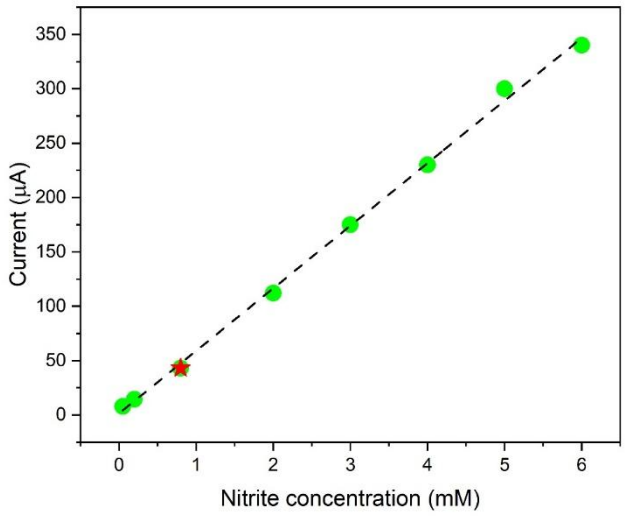


Figure 11. Calibration curves (blue dots and dashed red line) for $NO_2^-$ in 0.01 M PBS solution (pH 7) from 0.05 mM to 6 mM. The red star indicates the nitrite concentration (0.8 mM) measured after ammonia production.

## 9. Reproducibility and Repeatability Tests of the Sensor

The reproducibility and repeatability of the sensor were evaluated. Reproducibility refers to the consistency of sensor responses when measurements are performed using independently fabricated electrodes under the same conditions.

Repeatability refers to the consistency of measurements obtained with the same electrode over multiple trials, reflecting the sensor's short-term stability and operational performance. Both aspects are critical: reproducibility ensures that the fabrication process is reliable, while repeatability indicates the electrode's stability during practical use.

Reproducibility was assessed by measuring a series of nitrite concentrations (0.2, 0.5, 1, 2, 5, 10, 20, 30, 40, 50, and 60 µM) using three independently prepared electrodes (Figure 8). Each concentration was tested in triplicate, and the calculated RSD values, shown in Table 1, confirm the high reproducibility of the sensor response. These results demonstrate the robustness and reliability of the electrode functionalization procedure.

| **Concentration (µM)** | **RDS %** |
|---|---|
| 0.2 | 6.48% |
| 0.5 | 3.74% |
| 1 | 4.77% |
| 2 | 1.49% |
| 5 | 2.91% |
| 10 | 0.43% |
| 20 | 1.39% |
| 30 | 0.78% |
| 40 | 0.13% |
| 50 | 0.52% |
| 60 | 0.04% |

Table 1. RSD values obtained for reproducibility measurements

Repeatability was evaluated by performing five consecutive measurements of a 30 µM $NO_2^-$ solution using the same electrode. The sensor maintained stable performance up to the third measurement, after which a gradual decline was observed, with a 6.5% decrease in the anodic peak current compared to the first scan (Figure 12).

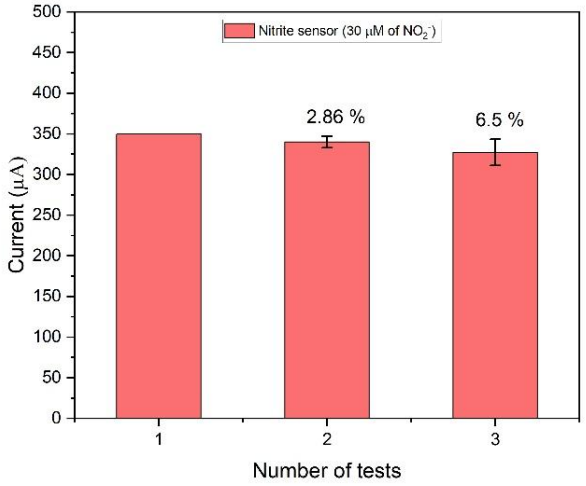


Figure 12. Repeatability test for Cu-Mn/C sensor. The oxidation peak current of the NO2- was recorded from the same sample over three consecutive measurements. Percentages represent the relative deviation of each measurement from the first.

These findings suggest a partial loss of electrochemical activity upon repeated use. However, considering that SPEs are typically designed as disposable devices, the ability of the electrode to maintain stable performance over multiple uses indicates promising short-term reusability, which may be advantageous for applications requiring several consecutive analyses without electrode replacement. To preserve sensor integrity, electrodes were stored in a dry, dark environment at room temperature when not in use. Between measurements, they were rinsed with deionized water to remove residual analyte and gently dried with inert gas. No regeneration treatments were applied, which may have contributed to the observed signal attenuation during repeated measurements.

## 10. Comparison with Literature and Discussion of Results

The nitrite detection performance of the developed sensor was compared with recent SPE-based electrochemical sensors reported in literature (Table 1) [2, 3, 25, 26].

**Table 2.** Comparison of this work with selected electrochemical sensing platforms for nitrite detection.

| Electrode | LoD | Linear Range | Application | Reference |
|---|---|---|---|---|
| SPE modified with CuO and $MnO_2$ (This work) | 71 nM | 0.2–60 µM | Drinking water | This work |
| SPCE modified with Cu-BDC frameworks and $Fe_2O_3$ NPs | 74 nM | 1–2000 µM | Mineral water | [26] |
| AuNP-modified SPCE | 0.38 µM | 5.0–100 µM | On-site detection in aqueous samples | [2] |
| SPE modified with $ZrO_2$@MWCNTs | 0.94 µM | 5.0–100 µM | Food and water samples | [3] |
| Polydopamine/Au NPs-modified SPCE | 1.98 µM | 10 to 500 µM | Processed meat samples in water | [27] |

The CuO-$MnO_2^-$ modified electrode developed in this work achieved an LoD of 71 nM, outperforming most previously reported sensors. Although a similar LoD of 74 nM was obtained wih a Cu-BDC/$Fe_2O_3$-modified SPCE [26], our sensor provides a more suitable linear detection range (0.2–60 µM) for monitoring nitrite levels in drinking water, where regulatory limits typically fall within the low micromolar range. By contrast, other sensors exhibit higher LoDs (0.38–1.98 µM)

and narrower linear ranges (5–10 μM), limiting their suitability for trace analysis [2,3,27]. Moreover, the use of inexpensive and non-toxic CuO and $MnO_2$ nanomaterials enhances the sutainability and practicality of the electrode modification strategy. These results confirm that the proposed sensor offers a highly sensitive, selective, and environmentally sustainable approach for nitrite detection in drinking water.

## CONCLUSION

The nitrite sensor (Cu-Mn/C), incorporating a CuO-$MnO_2$ composite, demonstrated a high sensitivity of 10.83 μA/μM, an ultralow LoD of 71 nM, and a wide linear range of 0.2–60 μM, thus meeting and surpassing the stringent requirements set by WHO and EU regulations for drinking water quality. The excellent analytical performance is attributed to the synergistic electrocatalytic activity of the CuO and $MnO_2$ nanostructures.

The sensor exhibited negligible interference from common water contaminants, excellent reproducibility, and acceptable repeatability for multiple measurements. Although a gradual decline in signal intensity was observed after repeated use, the sensor showed high reproducibility (maximum RSD 2.91%) and moderate repeatability. Further optimization of electrode stability could enhance its operational lifetime. Overall, the Cu–Mn/C sensor represents a sensitive, selective, and practical tool for reliable nitrite detection in environmental monitoring applications.

REFERENCES

[1] Picetti, R.; Deeney, M.; Pastorino, S.; Miller, M.R.; Shah, A.; Leon, D.A.; Dangour, A.D.; Green, R. Nitrate and nitrite contamination in drinking water and cancer risk: A systematic review with meta-analysis. *Environ. Res.* **2022**, *210*, 112988. https://doi.org/10.1016/j.envres.2022.112988.

[2] Adiraju, A.; Munjal, R.; Viehweger, C.; Al-Hamry, A.; Brahem, A.; Hussain, J.; Kommisetty, S.; Jalasutram, A.; Tegenkamp, C.; Kanoun, O. Towards Embedded Electrochemical Sensors for On-Site Nitrite Detection by Gold Nanoparticles Modified Screen Printed Carbon Electrodes. *Sensors* **2023**, *23*, 2961. https://doi.org/10.3390/s23062961.

[3] Rajab, N.; Ibrahim, H.; Hassan, R.Y.A.; Youssef, A.F.A. Selective Determination of Nitrite in Water and Food Samples Using Zirconium Oxide (ZrO2)@MWCNTs Modified Screen Printed Electrode. *RSC Adv.* **2023**, *13*, 21259–21270. https://doi.org/10.1039/D3RA03448H.

[4] Ramakrishnappa, T.; Sureshkumar, K.; Pandurangappa, M. Copper oxide impregnated glassy carbon spheres based electrochemical interface for nitrite/nitrate sensing. *Mater. Chem. Phys.* **2020**, *245*, 122744. https://doi.org/10.1016/j.matchemphys.2020.122744.

[5] Šljukić, B.; Banks, C.E.; Crossley, A.; Compton, R.G. Copper Oxide – Graphite Composite Electrodes: Application to Nitrite Sensing. *Electroanalysis* **2007**, *19*, 79–84. https://doi.org/10.1002/elan.200603708.

[6] Zhang, L.; Yuan, F.; Zhang, X.; et al. Facile synthesis of flower like copper oxide and their application to hydrogen peroxide and nitrite sensing. *Chem. Central J.* **2011**, *5*, 75. https://doi.org/10.1186/1752-153X-5-75.

[7] Farina, R.; D'Arrigo, G.; Alberti, A.; Capuano, G.E.; Corso, D.; Screpis, G.A.; Coniglio, M.A.; Condorelli, G.G.; Libertino, S. Electrochemical Growth of Copper Crystals on SPCE for Electrocatalysis Nitrate Reduction. *Nanomaterials* **2024**, *14*, 1704. https://doi.org/10.3390/nano14211704.

[8] Farina, R.; D'Arrigo, G.; Alberti, A.; Scalese, S.; Capuano, G.E.; Corso, D.; Screpis, G.A.; Coniglio, M.A.; Condorelli, G.G.; Libertino, S. Copper Micro-Flowers for Electrocatalytic Sensing of Nitrate Ions in Water. *Sensors* **2024**, *24*, 4501. https://doi.org/10.3390/s24144501.

[9] Nozari-Asbemarz, M.; Amiri, M.; Imanzadeh, H.; Bezaatpour, A.; Nouhi, S.; Hosseini, P.; Wark, M.; Seifzadeh, D. Mixed metal oxides as efficient

electrocatalysts for water oxidation. *Int. J. Hydrog. Energy* **2022**, *47*, 5250–5259. https://doi.org/10.1016/j.ijhydene.2021.11.145.

[10] Farina, R.; Scalese, S.; Alberti, A.; Privitera, S.M.S.; Capuano, G.E.; Corso, D.; Screpis, G.A.; Reina, S.C.R.; Condorelli, G.G.; Coniglio, M.A. Electrocatalytical Nitrite Oxidation via Manganese and Copper Oxides on Carbon Screen-Printed Electrode. *Sensors* **2025**, *25*, 3764. https://doi.org/10.3390/s25123764.

[11] Srivastava, G.; Dalela, S.; Kumar, S.; Choudhary, B.; Alvi, P. Structural and Raman studies of MnO2 and Mn2O3 nano-particles. *Mater. Today Proc.* **2023**, *79*, 169–171.

[12] Jung, J.-Y.; Lee, J.; Kim, Y.; Shin, D.; Park, J.; Kim, S.; Byon, H.R.; Kim, H.; Song, H. Switching Methane Selectivity in Carbon Dioxide Electroreduction via Confining Copper(I) Oxide Nanocubes by Polyimine Shells. *ACS Catal.* **2025**, *15*, 2642–2653. https://doi.org/10.1021/acscatal.4c07082.

[13] Deng, Y.; Handoko, A.D.; Du, Y.; Xi, S.; Yeo, B.S. In Situ Raman Spectroscopy of Copper and Copper Oxide Surfaces during Electrochemical Oxygen Evolution Reaction: Identification of CuIII Oxides as Catalytically Active Species. *ACS Catal.* **2016**, *6*, 2473–2481. https://doi.org/10.1021/acscatal.6b00205.

[14] Zoolfakar, A.S.; Rani, R.A.; Morfa, A.J.; O'Mullane, A.P.; Kalantar-zadeh, K. Nanostructured copper oxide semiconductors: a perspective on materials, synthesis methods and applications. *J. Mater. Chem. C* **2014**, *2*, 1–17. https://doi.org/10.1039/C4TC00345D.

[15] Ghodselahi, T.; Vesaghi, M.; Shafiekhani, A.; Baghizadeh, A.; Lameii, M. XPS study of the Cu@Cu2O core-shell nanoparticles. *Appl. Surf. Sci.* **2008**, *255*, 2730–2734. https://doi.org/10.1016/j.apsusc.2008.08.110.

[16] Di Castro, V.; Polzonetti, G. XPS study of MnO oxidation. *J. Electron Spectrosc. Relat. Phenom.* **1989**, *48*, 117–123. https://doi.org/10.1016/0368-2048(89)80009-X.

[17] Su, X.; Feng, G.; Yu, L.; et al. In-situ green synthesis of CuO on 3D submicron-porous/solid copper current collectors as excellent supercapacitor electrode material. *J. Mater. Sci. Mater. Electron.* **2019**, *30*, 3545–3551. https://doi.org/10.1007/s10854-018-00632-y.

[18] Wang, J.; Zhang, D.; Nie, F.; et al. The role of MnO2 crystal morphological scale and crystal structure in selective catalytic degradation of azo dye. *Environ. Sci. Pollut. Res.* **2023**, *30*, 15377–15391. https://doi.org/10.1007/s11356-022-23223-1.

[19] Xu, M.; Bao, S.-J. Nanostructured MnO2 for Electrochemical Capacitor. In *Energy Storage in the Emerging Era of Smart Grids*; InTech: 2011. https://doi.org/10.5772/17978.

[20] Huang, W.; Li, J.; Xu, Y. Nucleation and Growth of Porous MnO2 Coatings Prepared on Nickel Foam and Evaluation of Their Electrochemical Performance. *Materials* **2018**, *11*, 716. https://doi.org/10.3390/ma11050716.

[21] Desai, M.A.; Vedpathak, A.S.; Bhapkar, A.R.; Saratale, G.D.; Sartale, S.D. An investigation of chemical and electrochemical conversion of SILAR grown Mn3O4 into MnO2 thin films. *J. Environ. Manag.* **2021**, *299*, 113564. https://doi.org/10.1016/j.jenvman.2021.113564.

[22] Malha, S.I.R.; Mandli, J.; Ourari, A.; Amine, A. Carbon black-modified electrodes as sensitive tools for the electrochemical detection of nitrite and nitrate. *Electroanalysis* **2013**, *25*, 2289–2297. https://doi.org/10.1002/elan.201300257.

[23] Ambaye, A.D.; Muchindu, M.; Jijana, A.; Mishra, S.; Nxumalo, E. Screen-printed electrode system based on carbon black/copper-organic framework hybrid nanocomposites for the electrochemical detection of nitrite. *Mater. Today Commun.* **2023**, *35*, 105567. https://doi.org/10.1016/j.mtcomm.2023.105567.

[24] Abdi, Z.; Vandichel, M.; Sologubenko, A.S.; Willinger, M.-G.; Shen, J.-R.; Allakhverdiev, S.I.; Najafpour, M.M. The importance of identifying the true catalyst when using Randles-Sevcik equation to calculate turnover frequency. *Int. J. Hydrog. Energy* **2021**, *46*, 1–10. https://doi.org/10.1016/j.ijhydene.2021.09.063.

[25] Marino, N.; Milazzo, R. G.; Farina, R.; Bongiorno, C.; Libertino, S.; Lombardo, S. A.; Privitera, S. M. S. High Performance Fe-MoS2 Electrocatalyst for Efficient Nitrate Reduction to Ammonia: Synergistic Design for Sustainable Ammonia Production. *ACS Sustain. Chem. Eng.* 2025, DOI pending.

[26] Reyter, D.; Bélanger, D.; Roué, L. Study of the electroreduction of nitrate on copper in alkaline solution. *Electrochim. Acta* **2008**, *53*, 5977–5984. https://doi.org/10.1016/j.electacta.2008.03.008.

[27] Algethami, F.K.; Rabti, A.; Mastouri, M.; Abdulkhair, B.Y.; Ben Aoun, S.; Raouafi, N. Highly sensitive capacitance-based nitrite sensing using polydopamine/AuNPs-modified screen-printed carbon electrode. *RSC Adv.* **2023**, *13*, 21336–21344. https://doi.org/10.1039/D3RA03898J.

# CHAPTER 4

# AMMONIUM ION SENSING

## 1- Introduction and State of the Art

Ammonium ions represent the reduced form of nitrogen and primarily originate from the decomposition of nitrogen-containing organic matter or the application of fertilizers. In aqueous environments, ammonium exists in equilibrium with free ammonia ($NH_3$), a toxic compound to aquatic organisms [1]. Moreover, the presence of ammonium in water often indicates of recent contamination from fecal or organic waste sources. Among the various approaches for the ammonium ion quantification, electrochemical detection via SPEs offers the advantages of real-time monitoring, low cost, high sensitivity, and selectivity. Korent et al. reported an ammonia sensor for biological fluids based on polyaniline (PANi) as the conducting polymer, combined with commercially available drop-cast gold nanoparticles. The device operated at neutral pH in phosphate-buffered saline, achieving a limit of detection of 1.44 μM, with a broad dynamic range of 51 μM – 510 mM. The synergy between the conductive polymer and gold nanoparticles enhanced electron transfer kinetics, providing a high density of active sites for ammonia adsorption and oxidation, ensuring reliable operation in protein-rich biological samples [2]. Zhybak et al. developed an electrocatalytic composite sensor based on PANi/Nafion/$Cu_2O$-modified SPE for ammonium ion detection in human serum. The sensor achieved a LoD of 0.50 μM and a linear range of 1 – 1000 μM when operated by amperometry at −0.45 V vs. Ag/AgCl. The inclusion of Nafion imparted selective ion-exchange properties, while $Cu_2O$ nanoparticles further enhanced the electrocatalytic reduction of ammonium, improving both selectivity and sensitivity in the presence of interfering species commonly found in serum [3]. Wang et al. introduced an electrochemical enzyme biosensor for ammonium ions in aquaculture water, employing a SPCE modified with gold

nanoparticles and polymethylene blue. This configuration exploited the redox mediation properties of polymethylene blue together with the high surface area of AuNPs to facilitate efficient electron transfer and enzyme immobilization. The sensor achieved a LoD of 0.65 μM and a linear detection range of 0 – 300 μM, making it suitable for monitoring ammonium levels in aquatic environments [4].

This chapter presents the development of two SPEs-based electrochemical sensors for ammonium ions detection in water, using electropolymerized and commercial PANi combined with electrodeposited Au NPs.

## 2- Materials and Methods

Two amperometric sensors were fabricated for the detection of ammonium ions in water by using two commercial SPEs. Specifically:

- One SPE featured a carbon screen-printed working electrode
- One SPE incorporated a polyaniline/carbon (PANI/C) screen-printed working electrode.

Both sensors have a counter electrode of carbon ink, and a silver ink reference electrode.

The carbon substrate was selected for its excellent conductivity and compatibility with electrochemical modifications. Polyaniline (PANI) is a p-type semiconductor, where most charge carriers are holes. The $\pi\pi$ and $\pi\pi^*$ orbitals serve the role of valence and conduction bands, respectively. The energy difference between $\pi\pi$ and $\pi\pi^*$ corresponds to the polymer's band gap [5-7]. Figure 1 depicts the structural formulas and redox states of PANI. At the top, the general polymer backbone is shown, with varying ratios of reduced and oxidized units. The subsequent structures represent the principal redox forms of PANI: the blue pernigraniline base and its salt, the violet emeraldine base and the green

emeraldine salt, and finally the colorless leucoemeraldine. These forms are interconverted by processes of protonation (addition or removal of acid, HA) and electron transfer (oxidation or reduction), as indicated in the figure. Among these, the emeraldine salt, which is typically green, is recognized as the most conductive form and is therefore widely utilized in electrochemical sensing applications due to its favorable combination of conductivity and stability.

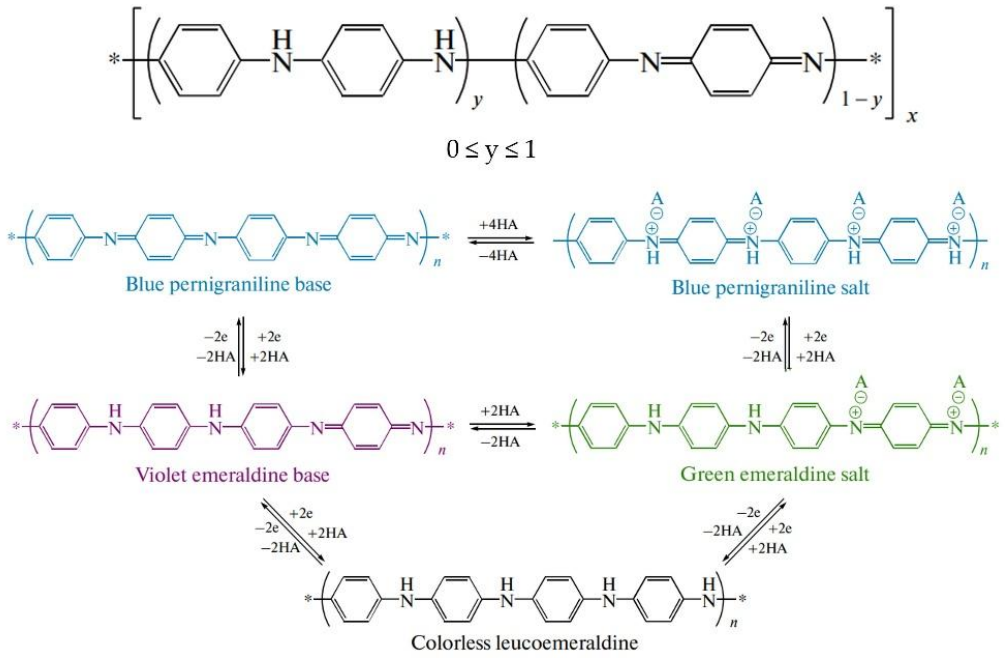


Figure 1. Redox states of polyaniline.

The PANI and Au NPs combination was chosen for their synergistic properties: PANI, a proton-conducting polymer, provides selective interaction with $NH_4^+$ ions through redox-mediated deprotonation; while Au NPs enhance electron transfer, catalytic activity, and electrochemical stability [8-10].

Two strategies were employed for their fabrication:

- The Au/PANI/C working electrode was fabricated by electrodeposition of Au NPs with cyclic voltammetry onto a commercial PANI/C electrode

- the Au/PANIep/C working electrode was fabricated by electrodeposition of Au NPs onto a CV-electropolymerized PANI electrode.

The electrochemical performance of both sensors was investigated by chronoamperometry (CA).

## 3- Fabrication of Au/PANI/C and Au/PANIep/C Electrodes

Figure 2 summarizes the functionalization process of the two different electrodes. Electropolymerization of PANI on the C working electrode (WE, 4 mm diameter) was performed using 0.1 M aniline monomer in a 1 M HCl solution. Traditionally, hydrochloric acid (HCl) with sulfuric acid ($H_2SO_4$), or chloric acid ($HClO_3$) is used as a dopant in the synthesis of conductive PANI. In acid doping, the interaction of polymeraldine with HCl induces protonation at imine sites, yelding polymeraldine salt. Low temperatures and high dopant concentrations favor a faster polymerization process and the production of a thicker polymer film. Therefore, electropolymerization of aniline was carried out at room temperature in a relatively low HCl concentration (1 M).

Electrodeposition was performed on the WE by CV using 15 scan cycles over a potential range of −0.3 V to 1.0 V, with a scan rate of 0.05 $Vs^{-1}$ [2].

Gold electrodeposition on both the electroplymerized PANI (PANIep/C) and the commercial PANI/C working electrodes (4 mm diameter) was performed in 0.1 M $HAuCl_4$ dissolved in 1 M HCl solution. The process was carried out by CV with 5 scan cycles over a potential ranging from 0.0 V to 1.0 V, at a scan rate of 0.05 $Vs^{-1}$ [11].

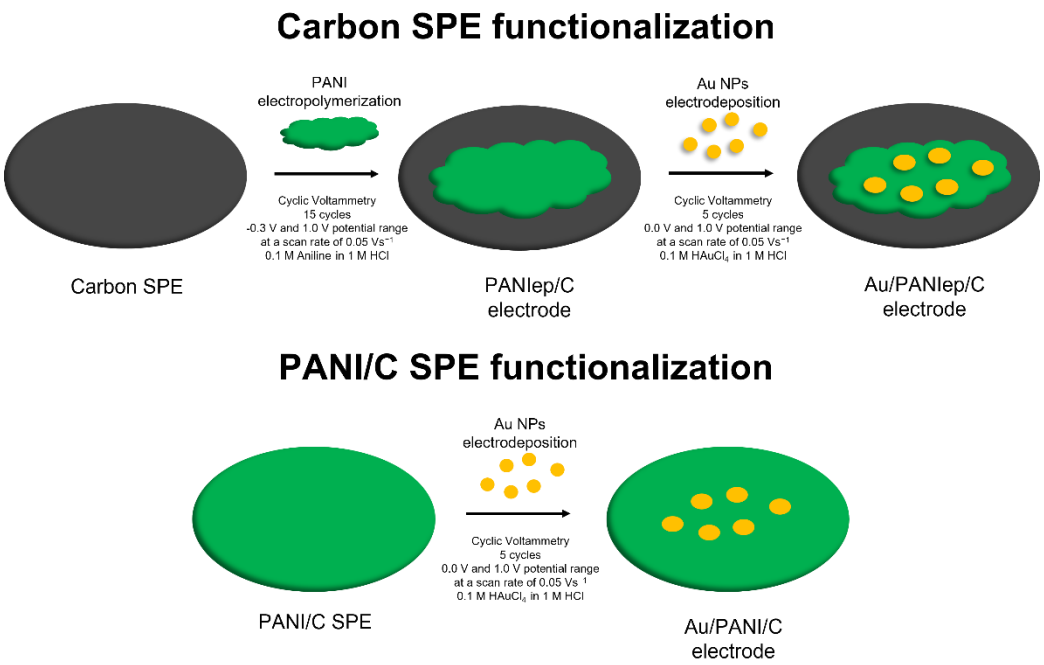


Figure 2. Scheme of the functionalization process of the two different electrodes: Au electrodeposited on PANIep/C (Au/PANIep/C) and Au electrodeposited on commercial PANI/C (Au/PANI/C).

## 4- Morphological and compositional characterization of Au/PANI/C and Au/PANIep/C Electrodes

SEM analysis was performed to investigate the morphological differences between the two developed electrodes.

Figure 3a shows the surface of the bare C WE, characterized by a flake-like structure typical of the screen-printing process. After CV electropolymerization, the surface of the PANIep/C WE (Figure 3b) exhibited nanogranular nucleation of PANIep, which grew into nanofibers. These nanofibers did not fully cover the carbon substrate but formed discrete islands, likely due to the irregular morphology of the screen-printed carbon surface.

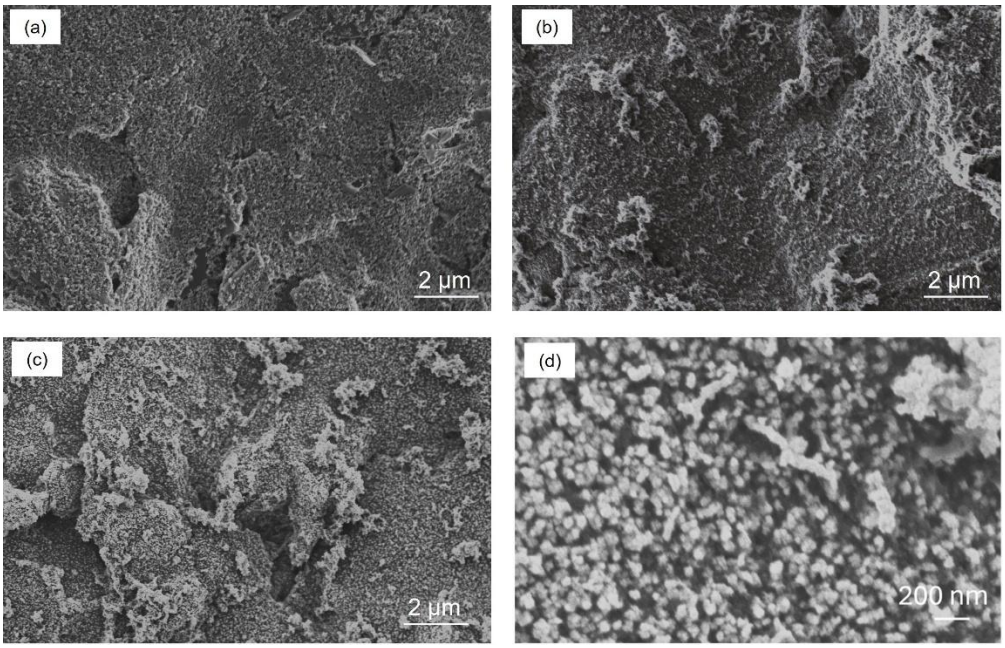


Figure 3. SEM images of (a) carbon bare SPE; (b) electrodeposited PANI on carbon SPE; (c) Au electrodeposited on PANIep/C; (d) magnification of Au NPs on PANIep/C.

The Au/PANIep/C electrode (Figure 3c) displayed a granular morphology composed of particles of different sizes (30–60 nm, Figure 3d) and surface textures. Morphologically, Au NPs did not disrupt the nanogranular and nanofibrous PANIep structure, but were uniformly distributed across the WE surface, providing complete coverage of the exposed carbon regions.

The commercial PANI/C WE (Figure 4a) exhibited a uniform and porous polyaniline film on the carbon substrate. This conductive PANI film provided an increased surface area, enabling effective electrodeposition of Au NPs. SEM images in Figure 4b revealed a dense and homogeneous layed of Au NPs with smaller particle sizes (20–30 nm, Figure 4c) compared to those formed on the PANIep/C electrode.

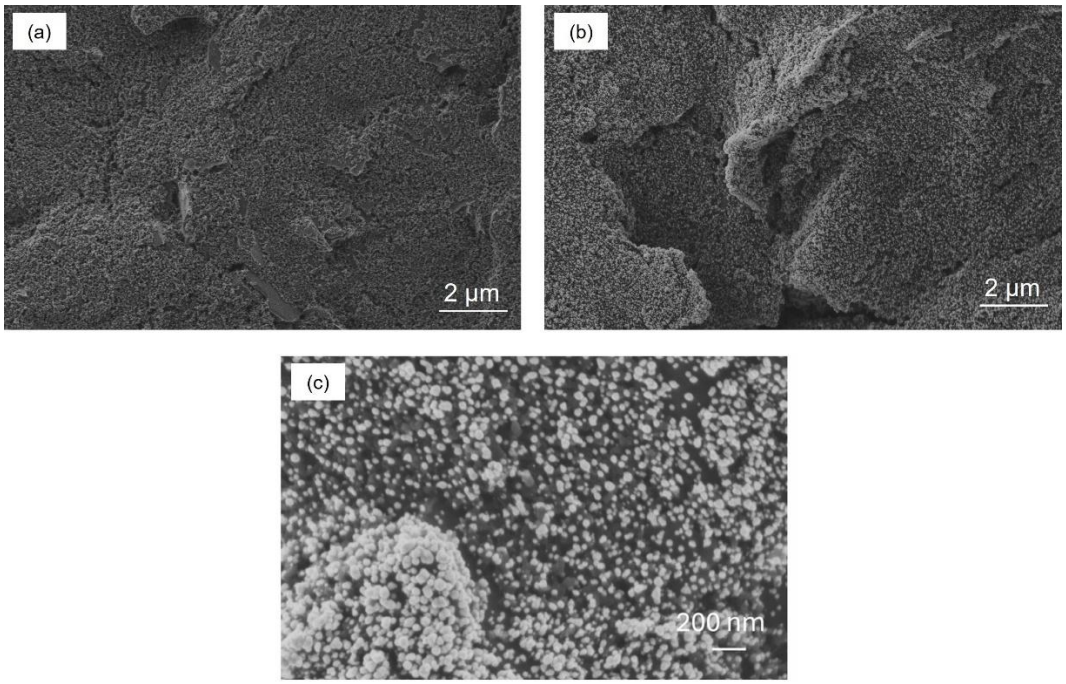


Figure 4. SEM images of (a) PANI/C bare SPE; (b) Au electrodeposited on commercial PANI/C SPE; (c) magnification of Au NPs on PANI/C.

Nanoparticles of different sizes exhibit distinct surface-to-volume ratios, significantly influencing their chemical reactivity. in general, smaller Au NPs provide a larger surface area per unit mass compared to larger ones, resulting in enhanced catalytic activity. The size distribution of electrodeposited Au nanoparticles is influenced by the nature of the underlying substrate. The microgranular PANIep offers heterogeneous anchoring sites, leading to variable NP size and orientation. On the other end, the continuous PANI film of commercial electrodes provides a more homogeneous and continuous matrix, favoring uniform NPP dispersion. Consequently, exposed carbon regions on PANIep/C promoted the nulcleation of larger gold nanoparticles compared to commercial PANI/C film.

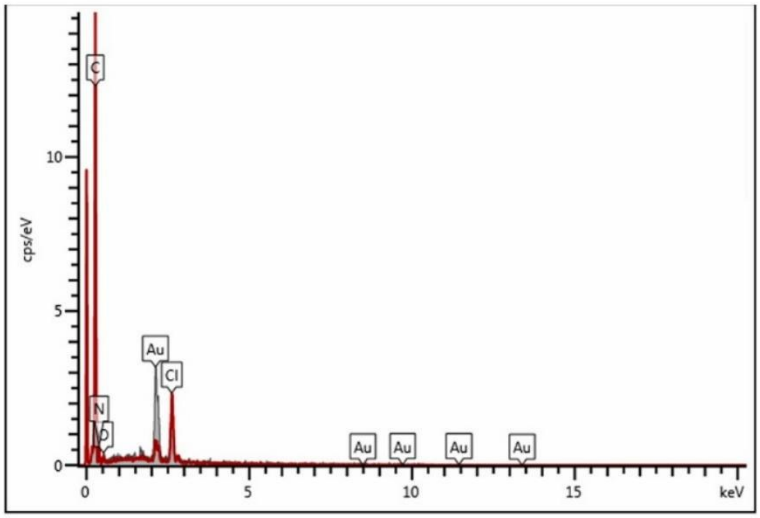


| Element | Wt% on top of Au NP | Wt% on a "clean" surface |
|---|---|---|
| C | 62.4 | 72.4 |
| Au | 19.3 | 5.1 |
| N | 11.8 | 14.1 |
| Cl | 4.9 | 6.3 |
| O | 1.7 | 2.0 |

Figure 5. EDS analysis of AuNPs: grey spectrum acquired on Au nanoparticles; red spectrum acquired from a surface region without visible AuNPs.

Energy-dispersive X-ray spectroscopy (EDS, Figure 5) confirmed the formation of AuNPs on both electrode types. The overall Au content was about 5% across the PANI.modified surfces, with local peaks up to 19% where AuNPs were clearly visible in the SEM images.

## 5- Electrochemical characterization of Au/PANI/C and Au/PANIep/C Electrodes

The voltammograms shown in Figure 6 display the characteristic oxidation peaks of PANI ($a_1$ = 0.24 V and $a_2$ = 0.81 V vs Ag) and the corresponding reduction peaks (c1 = 0.52 V, $c_2$ = 0.30 V, and $c_3$ = −0.1 V vs Ag). During the initial cycles

of electropolymerization, an additional PANI oxidation peak appears at 0.97 V vs Ag, which is later overlapped by the emeraldine oxidation peak ($a_2$ = 0.81 V vs Ag) [12] as the number of deposition cycles increases. Specifically, peak $a_1$ corresponds to the oxidation of leucoemeraldine to emeraldine, while peak $a_2$ indicates the oxidation of emeraldine to pernigraniline. Peaks $c_1$ and $c_2$ are associated with the reduction of pernigraniline to emeraldine, and peak $c_3$ corresponds to the reduction of emeraldine to leucoemeraldine [13-16]. In acidic media, polyaniline initially exists in its fully reduced form (leucoemeraldine) and undergoes two distinct redox transitions: first to the half-oxidized form (emeraldine), and then to the fully oxidized form (pernigraniline). The oxidation peaks ($a_1$, $a_2$) and reduction peaks ($c_1$, $c_2$) together definetwo redox couples: $a_1/c_2$ corresponds to leucoemeraldine ↔ emeraldine transition, and $a_2/c_1$ to emeraldine ↔ pernigraniline transition. The final product of electrochemical polymerization via cyclic voltammetry in HCl is HCl-doped PANI obtained in the form of the green emeraldine salt [13-15].

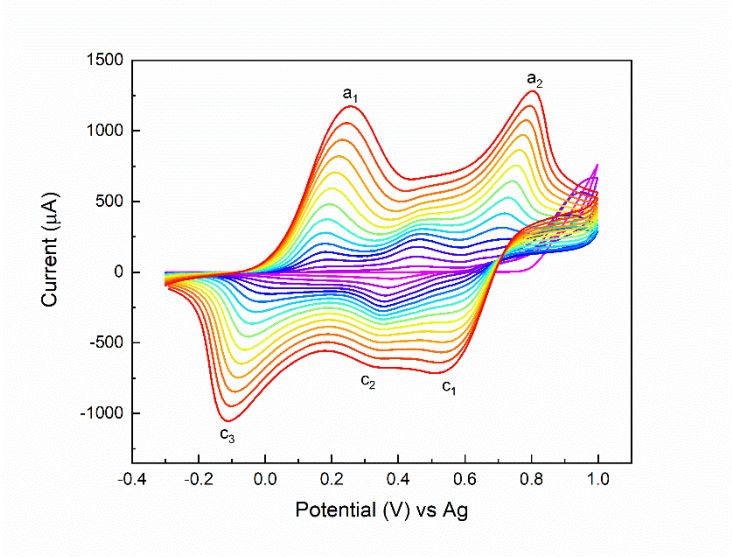


Figure 6. Cyclic voltammograms of polyaniline electropolymerization in 1 M HCl, potential ranging from −0.3 to 1.0 V, scan rate of 50 mV $s^{-1}$.

HCl concentration plays a crititcal role in determining the morphology of electropolymerized PANI. Proton doping with HCl promotes the delocalization of diiminoquinone–diaminobenzene states within the polymer, stabilizing emeraldine salt form of PANI. In its undoped state (emeraldine base), polyaniline is electrically neutral and poorly conductive; upon acid doping, however, it becomes highly conductive due to proton induced charge delocalization [13].

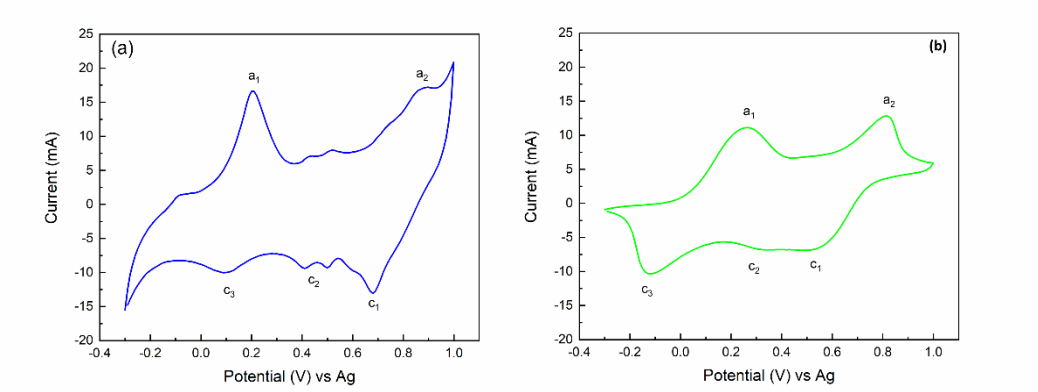


Figure 7. Cyclic voltammograms in 1 M HCl to a potential ranging from −0.3V to 1.0 V with a scan rate of 50 mV $s^{-1}$: (a) Au/PANI/C; (b) Au/PANIep/C.

The cyclic voltammograms in Figure 7 illustrate the characteristic redox behavior of polyaniline in both Au/PANI/C and Au/PANIep/C electrodes, exhibiting distinct electrochemical signatures attributed to polymer transitions and gold nanoparticle interactions. In the Au/PANI/C electrode (panel a), cathodic peaks appear at slightly more negative potentials, consistent with the typical overpotential associated with PANI redox transitions. In contrast, the Au/PANIep/C electrode (panel b) exhibits similar redox features but with broader and more intense current responses, reflecting the porous, fibrillar morphology of electropolymerized PANI. This structure enhances mass transport, provides a larger electroactive surface area, and promotes stronger interactions with Au NPs.

In both systems, the incorporation of Au NPs facilitates redox transitions by enhancing electronic conductivity and reducing charge transfer resistance. This

effect is particularly pronounced in the Au/PANIep/C electrode, where Au NPs are more uniformly distributed within the electropolymerized matrix. Differences in peak potentials and current magnitudes underscore the critical role of polymer morphology and Au NP distribution in defining the electrochemical performance of these hybrid materials for sensing applications. The ammonium ion,with its tetrahedral structure centered on a nitrogen atom bonded to four hydrogens, carries a positive charge and is capable of forming hydrogen bonds with protonated amine groups, favoring strong interaction with doped PANI.$NH_4^+$ ions form hydrogen bonds with the protonated amine ($-NH_2^+$) sites of doped PANI, creating a cross-linked network through hydrogen bridges connecting the ion and polymer chains. Additionally, the positive charge of $NH_4^+$ electrostatically interacts with $-NH_2^+Cl^-$ groups, providing further stabilization. This specificity toward ammonium arises mainly from the stronger and more stable hydrogen bonds compared to other cations like $Na^+$, $K^+$, or $Ca^{2+}$, as well as from the steric and dimensional compatibility of $NH_4^+$'s tetrahedral geometry with the protonated amine sites. Moreover, the synergy between PANI and AuNPs enhances this interaction, as protonated PANI combined with the nanostructured gold surface forms a system capable of preferentially capturing ammonium ions over other cations. Binding of $NH_4^+$ to doped PANI induces a change in charge density along the polymer chain, altering its conductivity. This interaction causes an electrochemically detectable change in the electrical resistance of the polymer matrix.

## 6- Electrochemical Sensors Performance for Ammonium Ion Detection and Interferences Tests

Since PANI undergoes redox and protonation reactions during potential scans CA was employed as the detection method. In amperometry, the current generated at

a fixed potential is recorded and correlated with the analyte concentration. To determine the optimal oxidation or reduction potential of the analyte, preliminary cyclic voltammetry must be performed [16-18].

The electrochemical study focused on the first oxidation peak (a1) corresponding to the leucoemeraldine ↔ emeraldine transition), since the pernigraniline form is unstable due to the quinoid-imine structure [13,14]. Thus, the active form of PANI for $NH_4^+$ detection is the emeraldine salt (protonated half-oxidized form), obtained after CV polymerization in HCl. The operating potentials selected were 0.25 V for Au/PANI/C and 0.35 V for Au/PANIep/C, as determined from their cyclic voltammograms (Figure 7). The redox couple a1/c2 represents a diffusion-controlled process, and $NH_4^+$ ions are known to form strong hydrogen bonds with polyaniline, occupying available protonation sites [19,20]. The resulting PANI·$NH_4^+$ complex induces an immediate increase in oxidation current.

Upon applying the potential, $NH_4^+$ undergoes oxidation, supplying electrons and protons that simultaneously reduce emeraldine base back to a protonated, conductive form, while oxidation continue under the applied bias [13]. After the depletion of $NH_4^+$ and deprotonation of PANI, the current decays to its baseline value and stabilizes, producing a transient amperometric signal. The presence of Au NPs further enhances detection by improving charge transfer and increasing the conductivity of PANI [21]. Owing to its p-type conduction, PANI forms efficient ohmic contacts with Au (work function 5.2 eV), facilitating rapid charge exchange at the polymer–metal interface. The polymer–metal contact is defined by both the metal's Fermi level lowest unoccupied molecular orbital positions [22–24].

The electrochemical performance of the two sensors, Au/PANI/C and Au/PANIep/C, for the detection of $NH_4^+$ in aqueous solution was evaluated. Amperometric calibration curves (Figure 8 a,b) were obtained in 1 M HCl (ensuring $NH_4^+$ prevalence over $NH_3$, with a pKa of 9.2 at 25 °C) for concentrations ranging from 0.35 µM to 7 µM. Both electrodes responded to

increasing $NH_4^+$ concentrations, though with different behaviors. The Au/PANIep/C electrode (green triangles) exhibited a smooth, linear, and high reproducible response even at submicromolar concentrations, reflecting efficient charge transfer and homogeneous nanoparticle distribution, with a high number of active sites. In contrast, the Au/PANI/C electrode (blue squares) displayed a lower sensitivity at low concentrations (<2 µM), with greater variability, and only showed a marked increase above 2 µM, suggesting that the PANI film may either limit the $NH_4^+$ access to the active sites or slow down ion diffusion.

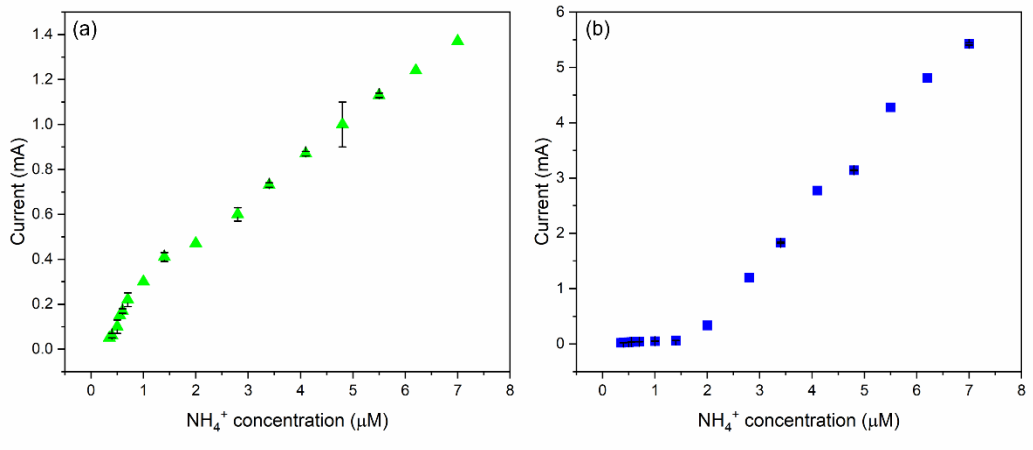


Figure 8. Calibration curves for $NH_4^+$ detection: (a) Au/PANIep/C (green triangles): (b) Au/PANI/C (blue squares) electrodes. Calibration range: 0.35 -7 µM.

The data reveal distinct behaviors for the two electrodes.

At higher concentrations (2–7 µM), Au/PANI/C exhibited higher sensitivity (1.09 mA/µM) compared to its performance at low levels (0.03 mA/µM). Conversely, Au/PANIep/C demonstrated higher sensitivity in the low concentration range (0.34 mA/µM), but saturation effects limited its response at higher levels (0.18 mA/µM) (Figure 9a–b). The calibration curves were split, as previously reported in the literature [13,25,26].

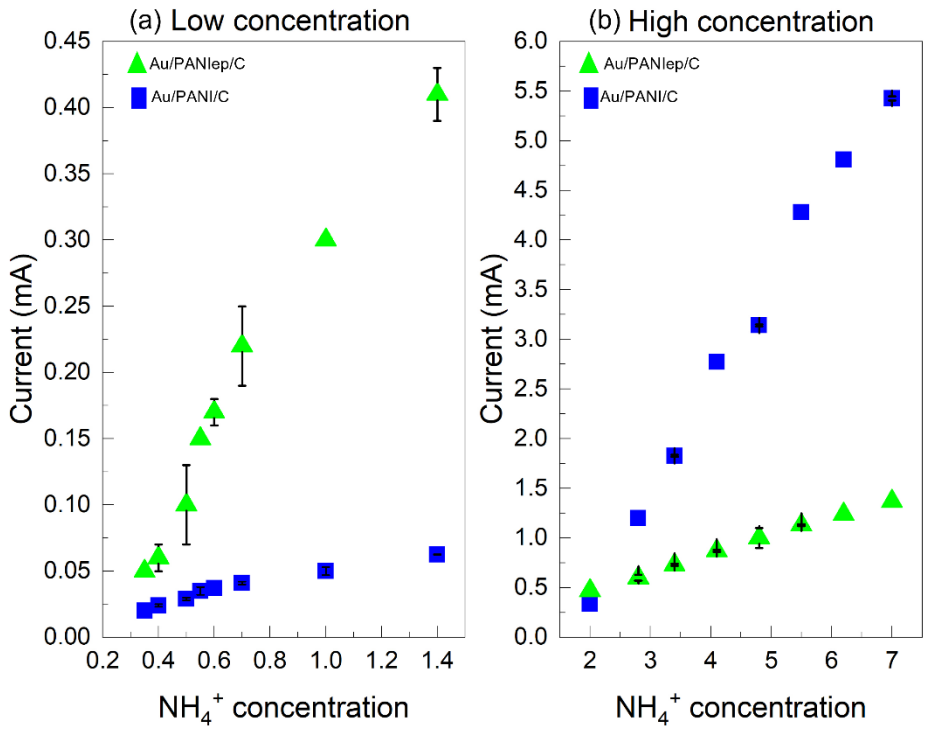


Figure 9. Calibration curves for $NH_4^+$ detection with Au/PANIep/C (green triangles) and Au/PANI/C (blue squares) electrodes: (a) low concentration range (0.35 -1.5 µM); (b) high concentration range (2-7 µM).

This behavior can be explained by the electrode morphology. The commercial PANI-coated carbon electrode performs poorly at low concentrations because undoped PANI restrict $NH_4^+$ diffusion to the active sites, while at higher concentrations diffusion limitations are overcome. By contrast, the nanogranular structure of electropolymerized PANI allows greater accessibility of $NH_4^+$ to protonation sites at low concentrations but saturates rapidly when these sites become fully occupied at higher levels.

In summary, the polyaniline distribution on the carbon electrode significantly affects the sensor sensitivity and dynamic range.

Finally, interference tests demonstrated that the developed electrodes are selective for ammonium ions over nitrate and nitrite. Reduction of for nitrate and nitrite requires much more negative potentials than those applied for ammonium detection. At the potentials optimized for $NH_4^+$ sensing (0.25 V and 0.35 V), and therefore these interferents remain electrochemically inactive under operating conditions (potentials below their activation barriers). The absence of significant faradaic processes for $NO_3^-$ and $NO_2^-$ under these conditions ensures that the sensor's response is specific to ammonium ions, minimizing the risk of false positives or analytical interference. Additionally, the selectivity of PANI arises from its chemical structure and properties. In its emeraldine salt form, PANI is a conductive polymer matrix that supports fast electron transfer for certain analytes, such as ammonium ions, but does not promote the adsorption or activation of more oxidized nitrate/nitrite species. The presence of Au NPs further enhances $NH_4^+$ detection by offering abundant active sites and facilitating charge transfer, but does not lower the activation barrier for $NO_3^-$ or $NO_2^-$ reduction at the applied potentials, ensuring high specificity of the sensor.

## 7- Reproducibility and Repeatability Tests of the Sensors

The reproducibility and repeatability of the sensors were evaluated. Reproducibility refers to the consistency of sensor responses when measurements are performed using independently fabricated electrodes under the same conditions. Repeatability refers to the consistency of measurements obtained with the same electrode over multiple trials, reflecting the sensor's stability and performance over time. Both parameters are critical: reproducibility ensures that the fabrication process is reliable, while repeatability indicates the sensor's operational stability during use.

Reproducibility was assessed by measuring a series of ammonium ion concentrations using three independently prepared electrodes (Figure 9). Each concentration was measured in triplicate. The calculated RSDs values for both electrodes as shown in table 3. Overall, the electrodes exhibits good reproducibility, with a maximum relative standard deviation of 5.94% for Au/PANIep/C and 3.68% for Au/PANI/C. These results demonstrate the reliability and consistency of the electrode functionalization procedure.

| **Concentration (µM)** | **Au/PANIep/C RDS %** | **Au/PANI/C RDS %** |
|---|---|---|
| 0.35 | 0.00% | 0.00% |
| 0.4 | 2.43% | 1.67% |
| 0.5 | 5.94% | 1.88% |
| 0.55 | 0.28% | 3.50% |
| 0.6 | 2.70% | 0.00% |
| 0.7 | 5.48% | 2.01% |
| 1 | 0.00% | 3.68% |
| 1.4 | 3.84% | 0.88% |
| 2 | 0.00% | 0.00% |
| 2.8 | 0.36% | 0.00% |
| 3.5 | 0.15% | 3.57% |
| 4.1 | 0.26% | 0.00% |
| 4.8 | 0.54% | 3.51% |
| 5.5 | 0.21% | 0.00% |
| 6.2 | 0.00% | 0.00% |
| 7 | 0.00% | 2.37% |

Table 1. RSD values obtained for reproducibility measurements

Repeatability tests were carried out using the same Au/PANI/C and Au/PANIel/C electrodes for six consecutive measurements with the same $NH_4^+$ solution. A concentration of 2 µM, above the sensitivity transition threshold of both electrodes, was selected (Figure 10). After each measurement, the electrodes were rinsed with distilled water and dried in an inert gas. The standard deviation was calculated by comparing the subsequent current peak values with the first measurement. The results are summarized in Table 3.

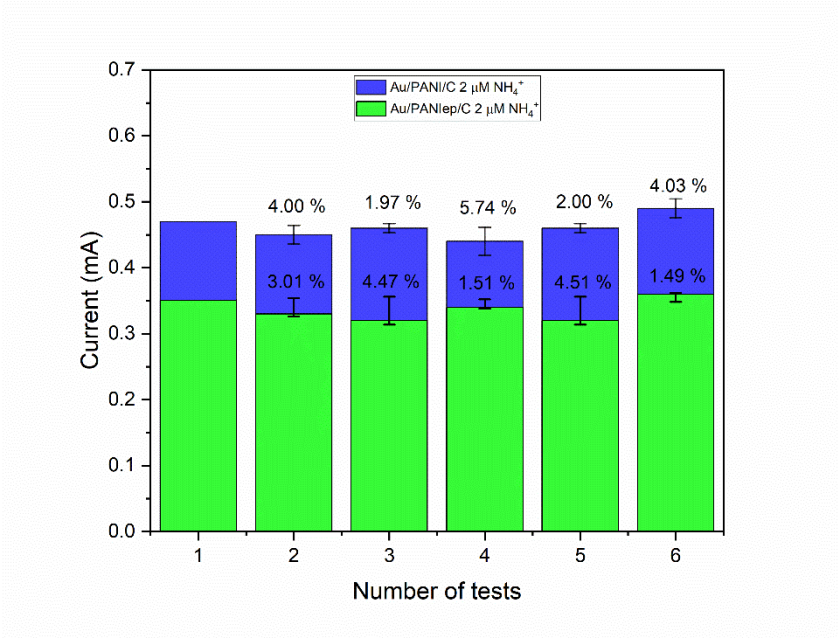


Figure 10. Repeatability test for Au/PANIep/C electrode (green bars), and Au/PANI/C electrode (blue bars) at 2 µM $NH_4^+$ concentration. The oxidation peak current of $NH_4^+$ was acquired from the same sample over six repeated measurements.

These results confirm the high operational repeatability of the sensors and the electrochemical stability of the PANI-based materials under continuous measurement cycles. The low RSD values across repeated measurements indicate minimal drift and excellent stability of the current response, even after the

electrode cleaning and re-immersion in the analyte solution. Moreover, the consistent signal recovery after each wash step highlights the structural robustness and chemical resilience of the PANIep-modified electrode. The absence of significant signal degradation suggests that the active polymer layer retains its electrochemical activity and structural integrity after repeated use.

| | **Tests in a 2 µM $NH_4^+$ solution** | | | | | |
|---|---|---|---|---|---|---|
| | 1 | 2 | 3 | 4 | 5 | 6 |
| **Au/PANIep/C** **RSD %** | - | 3.01% | 4.47% | 1.51% | 4.51% | 1.49% |
| **Au/PANI/C** **RSD %** | - | 4.00% | 1.97% | 5.74% | 2.00% | 4.03% |

Table 3. RSD values obtained for repeatability measurements.

## 8- Comparison with Literature and Discussion of Results

The performance of the developed sensors for ammonium ion detection appears promising when compared with recent SPE-based electrochemical sensors reported in literature (Table 1) [2-4]. The enhanced performance of the developed sensor is attributed to the synergistic interaction between polyaniline and gold nanoparticles, which facilitates efficient electron transfer and increases the density of electroactive sites for ammonium ion adsorption. This synergy contributes to a low background current and ultra-trace-level detection capability. Importantly, unlike other sensing platforms that incorporate enzymes, surfactants, or complex composites, the Au/PANIep/C sensor relies solely on inorganic nanoparticles and a conductive polymer. Both are chemically stable and can be easily fabricated via electrodeposition, simplifying the preparation process while

enhancing reproducibility and long-term operational stability, avoiding issues related to enzyme degradation.

Table 1. Comparison of this work with selected literature reports on SPE-based electrochemical platforms for ammonium ions detection.

| Electrode | LoD | Linear Range | Application | Reference |
|---|---|---|---|---|
| SPCE modified with $Pani_{ep}$ and Au NPs | 0.03 µM | 0.35-1.5 µM | Drinking water | This work |
| Pani SPE modified with Au NPs | 0.34 µM | 2.0-7.0 µM | Drinking water | This work |
| SPEC modified with AuNPs and polymethylene blue | 0.65 µM | 0–300 µM | Aquaculture water | [4] |
| SPE modified with PANi/Nafion/$Cu_2O$ | 0.50 µM | 1.0–1000 µM | Human Serum | [3] |
| Polydopamine/Au NPs-modified SPCE | 1.44 µM | 51 µM to 510 mM | Biological fluids | [2] |

While other systems may be optimized for complex biological matrices (e.g., serum or urine), they often lack the sensitivity required for detecting ammonium at the trace concentrations relevant to drinking water safety standards. In contrast, our sensor achieves a balance between high sensitivity, operational simplicity, and applicability to real-world scenarios.

Overall, the developed sensors provide a robust and scalable platform with superior performance compared to comparable systems, enabling accurate, reliable, and enzyme-free detection of ammonium ions in drinking water.

## CONCLUSION

Two fabrication strategies were implemented via cyclic voltammetry electrodeposition of Au NPs: (i) on a commercial PANI/C electrode (Au/PANI/C) and (ii) on a CV-electropolymerized PANIep/C electrode (Au/PANIep/C). In both cases, Au NPs enhanced the electrical conductivity of PANI and facilitated charge transfer during electrochemical reactions. The distribution of PANI on the carbon substrate significantly influenced the sensitivity and dynamic range for $NH_4^+$ detection in amperometry. The electrodes were tested in the concentration range 0.35 – 7 µM $NH_4^+$ in 1 M HCl solution. Results indicate that the Au/PANI/C electrode performed better at higher $NH_4^+$ concentrations (LoD=0.34 µM), and worse at low $NH_4^+$ concentrations (LoD=0.01 µM), while the Au/PANIep/C electrode was more effective at low concentrations (LoD= 0.03 µM) than at higher concentrations (LoD=0.07 µM). Both electrodes showed good reproducibility (maximum RSD of 5.94% for Au/PANIep/C and 3.68% for Au/PANI/C), and repeatability tests confirmed consistent recovery of the working electrode signal after each measurement. These findings demonstrate the robustness, stability, and practical applicability of the developed sensors for ammonium ion detection in aqueous environments.

REFERENCES

[1] Edwards, T.M.; Puglis, H.J.; Kent, D.B.; López Durán, J.; Bradshaw, L.M.; Farag, A.M. Ammonia and aquatic ecosystems – A review of global sources, biogeochemical cycling, and effects on fish. *Sci. Total Environ.* **2024**, *907*, 167911. https://doi.org/10.1016/j.scitotenv.2023.167911

[2] Korent, A.; Trafela, Š.; Žagar Soderžnik, K.; Samardžija, Z.; Šturm, S.; Žužek Rožman, K. Au-decorated electrochemically synthesised polyaniline-based sensory platform for amperometric detection of aqueous ammonia in biological fluids. *Electrochim. Acta* **2022**, *430*, 141034. https://doi.org/10.1016/j.electacta.2022.141034

[3] Zhybak, M.T.; Vagin, M.Y.; Beni, V.; Liu, X.; Korpan, Y.I.; Turner, A.P.F. Direct detection of ammonium ion by means of oxygen electrocatalysis at a copper-polyaniline composite on a screen-printed electrode. *Microchim. Acta* **2016**, *183*, 1981–1987. https://doi.org/10.1007/s00604-016-1834-3

[4] Wang, C.; Wang, T.; Li, Z.; Xu, X.; Zhang, X.; Li, D. An Electrochemical Enzyme Biosensor for Ammonium Detection in Aquaculture Using Screen-Printed Electrode Modified by Gold Nanoparticle/Polymethylene Blue. *Biosensors* **2021**, *11*, 335. https://doi.org/10.3390/bios11090335

[5] Huang, J.; Virji, S.; Weiller, B.H.; Kaner, R.B. Polyaniline Nanofibers: Facile Synthesis and Chemical Sensors. *J. Am. Chem. Soc.* **2003**, *125*, 314–315. https://doi.org/10.1021/ja028371y

[6] Ramadin, Y.; Ahmad, M.; Zihlif, A.; Al-Haddad, R.; Makadsi, M.; Ragosta, G.; Martuscelli, E. Determination of the type of charge carriers in carbon fiber/polymer composite. *Polym. Test.* **1998**, *17*, 257–264. https://doi.org/10.1016/S0142-9418(97)00047-0

[7] Hashmi, A.S.K.; Hutchings, G.J. Gold Catalysis. *Angew. Chem. Int. Ed.* **2006**, *45*, 7896–7936. https://doi.org/10.1002/anie.200602454

[8] Chen, H.; Zhou, K.; Zhao, G. Gold nanoparticles: From synthesis, properties to their potential application as colorimetric sensors in food safety screening. *Trends Food Sci. Technol.* **2018**, *78*, 83–94. https://doi.org/10.1016/j.tifs.2018.06.001

[9] Zhang, G. Functional gold nanoparticles for sensing applications. *Nanotechnol. Rev.* **2013**, *2*, 269–288. https://doi.org/10.1515/ntrev-2013-0007

[10] Korent, A.; Žagar Soderžnik, K.; Šturm, S.; Žužek Rožman, K. A correlative study of polyaniline electropolymerization and its electrochromic behavior. *J. Electrochem. Soc.* **2020**, *167*, 106504. https://doi.org/10.1149/1945-7111/ab7b1e

[11] Farina, R.; Scalese, S.; Corso, D.; Capuano, G.E.; Screpis, G.A.; Coniglio, M.A.; Condorelli, G.G.; Libertino, S. Chronoamperometric Ammonium Ion Detection in Water via Conductive Polymers and Gold Nanoparticles. *Molecules* **2024**, *29*, 3028. https://doi.org/10.3390/molecules29133028

[12] MacDiarmid, A.G.; Manohar, S.K.; Masters, J.G.; Sun, Y.; Weiss, H.; Epstein, A.J. Polyaniline: Synthesis and properties of pernigraniline base. *Synth. Met.* **1991**, *41*, 621–626. https://doi.org/10.1016/0379-6779(91)90051-9

[13] Hassan, M.H.; Khan, R.; Andreescu, S. Advances in electrochemical detection methods for measuring contaminants of emerging concerns. *Electrochem. Sci. Adv.* **2022**, *2*, e2100184. https://doi.org/10.1002/elsa.202100184

[14] Fitriyana, F.K. Polyaniline-invertase-gold nanoparticles modified gold electrode for sucrose detection. *Indones. J. Chem.* **2015**, *15*, 226–233. https://doi.org/10.22146/ijc.13576

[15] Gvozdenovic, M.; Jugovic, B.; Stevanovic, J.; Grgur, B. Electrochemical synthesis of electroconducting polymers. *Hem. Ind.* **2014**, *68*, 673–684. https://doi.org/10.2298/HEMIND1406673G

[16] García-Miranda Ferrari, A.; Rowley-Neale, S.J.; Banks, C.E. Screen-printed electrodes: Transitioning the laboratory into the field. *Talanta Open* **2021**, *3*, 100032. https://doi.org/10.1016/j.talo.2021.100032

[17] Hanrahan, G.; Patil, D.G.; Wang, J. Electrochemical sensors for environmental monitoring: design, development and applications. *J. Environ. Monit.* **2004**, *6*, 657–664. https://doi.org/10.1039/b407872b

[18] Kuchena, S.F.; Wang, Y. Superior polyaniline cathode material with enhanced capacity for ammonium ion storage. *ACS Appl. Energy Mater.* **2020**, *3*, 11690–11698. https://doi.org/10.1021/acsaem.0c01543

[19] Crowley, K.; O'Malley, E.; Morrin, A.; Smyth, M.R.; Killard, A.J. An aqueous ammonia sensor based on an inkjet-printed polyaniline nanoparticle-modified electrode. *Analyst* **2008**, *133*, 391–399. https://doi.org/10.1039/b717776h

[20] MacDiarmid, A.G.; Yang, L.S.; Huang, W.S.; Humphrey, B.D. Polyaniline: Electrochemistry and application to rechargeable batteries. *Synth. Met.* **1987**, *18*, 393–398. https://doi.org/10.1016/0379-6779(87)90072-3

[21] Teo, C.H.; Karode, N.S.; Abid, K.; Rahman, F. Interfacial behaviour of polyaniline as an organic electronic material. *J. Phys. Chem. Solids* **2011**, *72*, 886–890. https://doi.org/10.1016/j.jpcs.2011.02.004

[22] Galiev, A.F.; Karamov, D.D.; Lachinov, A.A.; et al. Non-conjugated polymer films to monitoring strain deformation of metals and alloys. *J. Mater. Sci.: Mater. Electron.* **2024**, *35*, 976. https://doi.org/10.1007/s10854-023-07761-2

[23] Kahn, A. Fermi level, work function and vacuum level. *Mater. Horiz.* **2016**, *3*, 7–10. https://doi.org/10.1039/c5mh00304c

[24] Bhadra, S.; Chattopadhyay, S.; Singha, N.K.; Khastgir, D. Improvement of conductivity of electrochemically synthesized polyaniline. *J. Appl. Polym. Sci.* **2008**, *108*, 57–64. https://doi.org/10.1002/app.27497

[25] Zhang, L.; Liu, J.; Peng, X.; Cui, Q.; He, D.; Zhao, C.; Suo, H. Fabrication of a Ni foam-supported platinum nanoparticles-silver/polypyrrole electrode for aqueous ammonia sensing. *Synth. Met.* **2020**, *259*, 116257. https://doi.org/10.1016/j.synthmet.2019.116257

[26] Zhang, L.; Wan, J.; Li, J.; Cui, Q.; He, D.; Zhao, C.; Suo, H. Fabricating a self-supported electrode for detecting ammonia in water based on electrodepositing platinum-polypyrrole on Ni foam. *J. Electrochem. Soc.* **2020**, *167*, 027537. https://doi.org/10.1149/1945-7111/ab7b1e

## CONCLUSION

This doctoral thesis has demonstrated the development and characterization of three selective and sensitive electrochemical sensors for the detection of nitrate, nitrite, and ammonium ions in aqueous environments. By employing modified screen-printed electrodes as sensing platforms, this work presents low-cost, portable, and reliable alternatives to traditional analytical techniques. Each sensor was specifically engineered through electrode surface modification strategies to optimize performance for its target analyte. The nitrate sensor, based on Cu micro-flowers electrodeposited on carbon SPEs, achieved an excellent limit of detection of 0.87 µM and a broad linear range, attributing to its high surface area and catalytic activity. The nitrite sensor employed a dual-metal oxide approach (Cu-Mn/C), exploiting the synergistic redox behavior of $MnO_2$ and CuO, and demonstrated high selectivity, with a low detection limit of 0.071 µM and strong reproducibility. For ammonium ion detection, two Au-polyaniline composite electrodes (Au/PANI/C and Au/PANIep/C) were designed and compared, revealing that the electropolymerized PANI system provided superior sensitivity at ultra-trace concentrations (down to 0.03 µM). The sensors were validated not only in buffer systems but also in real water samples, including tap water and complex electrolytic matrices, confirming their operational robustness and negligible interference from common coexisting ions. Notably, the fabrication methods avoided the use of biological components (such as enzymes), which often present stability and storage limitation, thereby highlighting the practicality and durability of these electrochemical platforms. Overall, this work provides a solid foundation for future integration of such sensors into compact and decentralized water monitoring systems, with significant implications for environmental monitoring and public health protection.